CERN-PPE/91 – 24
5 February 1991

EUROPEAN ORGANIZATION FOR NUCLEAR RESEARCH

Performance of the ALEPH Time Projection Chamber

W.B.Atwood[1,f], T.Barczewski[4], L.A.T.Bauerdick[4,b], L.Bellantoni[8], E.Blucher[1], W.Blum[5], J.Boudreau[8], O.Boyle[3], D.Cinabro[8], J.Conway[8], G.Cowan[5], D.F.Cowen[8,a], I.Efthymiopoulos[2], P.Faure[1], Z.Feng[8], F.Fidecaro[6], B.Gobbo[7], A.W.Halley[3], S.Haywood[1], A.Jahn[5], R.C.Jared[8,e], R.P.Johnson[8], M.Kasemann[1,c], K.Kleinknecht[4], B.Leclaire[8], I.Lehraus[1], B.Lofstedt[1], T.Lohse[1], D.Lueke[1,c], A.Lusiani[6,b], P.S.Marrocchesi[6], J.May[1,c], T.C.Meyer[1], F.Morsani[6], A.Minten[1], J.Pater[8], D.Pollmann[d], M.Price[1], R.Richter[5], W.Richter[1], S.Roehn[4], L.Rolandi[7], A.Roth[1], H.Rotscheidt[1], D.Schlatter[1], M.Schmelling[4], H.Schmidt[4], J.Schroeder[5], R.Settles[5], F.Steeg[4], G.Stefanini[1], U.Stierlin[5], M.Takashima[1], W.Tejessy[1], I.Ten Have[3], J.Thomas[5], A.Vayaki[2], J.Wear[8], W.Wiedenmann[1], W.Witzeling[1], Sau Lan Wu[8]

[1] CERN, Geneva, Switzerland
[2] Nuclear Research Center Demokritos, Athens, Greece
[3] University of Glasgow, UK◇
[4] Institut für Physik, J.Gutenberg Universität, Mainz, Germany*
[5] Max-Planck-Institut für Physik und Astrophysik, Munich, Germany*
[6] Dipartimento di Fisica, Sezione INFN and Scuola Normale Superiore, Pisa, Italy
[7] Istituto di Fisica and Sezione INFN, Trieste, Italy
[8] University of Wisconsin, Madison, USA♯
[a] Now at California Institute of Technology, Pasadena, CA 91125, USA
[b] Now at CERN
[c] Present address DESY, Hamburg, Germany
[d] Present address Institut für Physik, Universität Dortmund, Germany
[e] Permanent address LBL, Berkeley, CA 94720, USA
[f] Permanent address SLAC, Stanford, CA 94309, USA
* Supported by the Bundesministerium für Forschung und Technologie
◇ Supported by the UK Science and Engineering Research Council
♯ Supported by the US Department of Energy, contract DE-AC02-76ER00881

Submitted to Nuclear Instruments and Methods A

Abstract

The performance of the ALEPH Time Projection Chamber (TPC) has been studied using data taken during the LEP running periods in 1989 and 1990. After correction of residual distortions and optimisation of coordinate reconstruction algorithms, single coordinate resolutions of 173 μm in the azimuthal and 740 μm in the longitudinal direction are achieved. This results in a momentum resolution for the TPC of $\Delta p/p^2 = 1.2 \cdot 10^{-3}$ (GeV/c)$^{-1}$. In combination with the ALEPH Inner Tracking Chamber (ITC), a total momentum resolution of $\Delta p/p^2 = 0.8 \cdot 10^{-3}$ (GeV/c)$^{-1}$ is obtained. With respect to particle identification, the detector achieves a resolution of 4.4% for the measurement of the ionisation energy loss.

1 Introduction

Charged particle tracking in the large 4π solid angle detector ALEPH is provided by a Time Projection Chamber (TPC) and a conventional cylindrical drift chamber called the Inner Tracking Chamber (ITC). Together with an electromagnetic calorimeter they are located inside a superconducting coil, which provides a magnetic field of 1.5 T, and are surrounded by a hadron calorimeter and muon chambers. A detailed description of the detector can be found elsewhere [1]. The motivation for a large TPC was to achieve the best possible momentum resolution together with ease in pattern recognition. The basic concept of a TPC was first proposed by D. R. Nygren [2]. Figure 1 shows an example of a fully reconstructed hadronic Z^0 decay.

The ALEPH TPC, with an outer diameter of 3.6 m and a length of 4.4 m, is the largest chamber of its kind. It is operated with an Argon-Methane (91:9) gas mixture at atmospheric pressure [3] and provides 21 three dimensional coordinate measurements for fully contained tracks. The ionisation charge is recorded at two end-plates by a system of proportional wire chambers with segmented cathode pad readout. Together with the two cylindrical field cages, they enclose the gas volume of 43 m^3. A graphite coated mylar membrane (thickness 25 μm) divides the chamber into two halves and is the central high voltage electrode. Eighteen wire chambers (or sectors) of three different shapes are mounted on each end-plate and are arranged in two concentric circles, the inner one having 6 and the outer one 12 sectors (see fig. 1).

The geometry was chosen such that stiff tracks passing along a sector boundary would have a sufficient number of coordinates for track reconstruction. Each end-plate has a total of 20502 cathode pads arranged in 21 circular pad rows and 3168 sense wires.

A charged particle traversing the sensitive volume of the TPC produces electrons and ions. The electrons from the primary ionisation drift up to 2.2 m towards one of the end-plates in an axial magnetic field of 1.5 T and an electrical field of 125 V/cm pointing parallel or antiparallel to the magnetic field vector in the two TPC halves. In the vicinity of a sense wire, the electrons create an avalanche and induce a signal on the cathode pads. The part of the ions created in the avalanche process which is drifting back towards the sensitive volume is neutralised at a gating grid. This grid is operated in synchronous mode [6] and prevents the build-up of space charge and related electric field distortions in the drift volume.

The pulse height induced on one pad is a superposition of pulse heights induced by avalanches of electrons approaching several adjacent wires. The signals on a pad row from a single track (a so-called cluster) extend in general over two or three neighbouring pads. Azimuthal coordinates are derived from the $r\varphi$ position of the recorded avalanche, whereas longitudinal coordinates are obtained from their measured drift times.

The signal processing is performed by Time Projection Digitizers (TPD) [4], which use flash-ADC's to sample the signals at a rate of 11.2 MHz during the 40 μs drift. Time Projection Processors (TPP) handle the readout and formatting of the data [5] and also perform the electronics calibration.

The electronics calibration is done by pulsing the field wires of the wire chambers and adjusting the tap points of the reference ladder for each flash-ADC such that all channels give linear and uniform response. The channel-to-channel uniformity has a width of $\sigma = 0.5\%$ for the electronics gain and $\sigma = 1.5$ LSB for the pedestal, thus avoiding the need to carry calibration constants for the 47340 channels to the analysis. The stability

of the electronics has proven to be excellent and recalibration is necessary only every few weeks.

2 The Pad Response Function

The coupling strength between cathode pads and sense wires depends on the distance between the pads and the electron avalanches and is described by the Pad Response Function (PRF). The pulse height on pad number i for a given azimuthal position x of the avalanche above the pad row can be described for the case where the track crosses the pad at zero angle by a Gaussian [7]

$$P_i(x) = C \exp\left(-\frac{(x - x_i)^2}{2\sigma^2_{\mathrm{PRF}}}\right) , \tag{1}$$

where x_i denotes the centre of the i-th pad. The chamber-specific pad response width σ_{PRF} is an essential parameter for the coordinate determination.

2.1 The Pad Response Width

The pad response width σ_{PRF} can be measured using two different algorithms for the cases of two- or three-pad clusters. For clusters containing two pads with pulse heights P_1 and P_2, σ_{PRF} can be derived according to (1) by fitting the track position x_{track} as a function of the measured ratio of pulse heights:

$$x_{\mathrm{track}} = \hat{\sigma}^2 \cdot \delta \cdot \ln\left(\frac{P_{i+1}}{P_i}\right) + x_i + \frac{\delta}{2} , \tag{2}$$

where $\hat{\sigma} = \sigma_{\mathrm{PRF}}/\delta$ and δ is the distance between two pad centres ($\delta = 0.67$ cm). If three pads with pulse heights P_1, P_2 and P_3, contribute to a cluster, σ_{PRF} can be directly related to the pulse heights:

$$\frac{1}{\hat{\sigma}^2} = \ln \frac{P_2^2}{P_1 P_3} . \tag{3}$$

The pulse heights P_1 and P_2 for the two-pad case (eq. 2) are of comparable size so that systematic effects of the pulse height measurements are less important, but the analysis depends on the knowledge of the azimuthal track position from the track fit. For the three-pad case (eq. 3), the track position does not enter, but the determination of $\hat{\sigma}^2$ is more affected by systematics of the pulse height measurements, since P_1 and P_3 are usually small compared to P_2.

The measurement of $\hat{\sigma}^2$ was performed with tracks from Z^0 decays using two- and three-pad clusters. Tracks were required to have more than 5 GeV/c momentum and at least 15 coordinates in the TPC. The angles of the tracks with respect to the pads and the wires are defined in figure 2. The experimental results with their parameterisations are presented in figure 3.

The pad response width is observed to be a function of three variables:

- The drift length l_{D}. Due to diffusion effects the recorded charge is spread out proportionally to the drift length, which implies $\hat{\sigma}^2 \propto l_{\mathrm{D}}$. Such a linear dependence of $\hat{\sigma}^2$ is confirmed by the data (figure 3a).

- The pad crossing angle α_p, which is the angle between the direction of the track projection onto the end-plate plane and the radial direction (see figure 2). The recorded charge cloud spreads in azimuthal direction over a length which is proportional to the pad height times $\tan\alpha_p$. Therefore, $\hat{\sigma}^2$ varies as $\tan^2\alpha_p$. This agrees with the data (figure 3b). The variation with α_p is the largest geometrical effect contributing to the pad response width. The size of the variation depends slightly on the cluster size on the pad row.

- The wire crossing angle α_w, which is the angle between the direction of the track projection onto the end-plate plane and the normal to the wire direction (compare figure 2). In the region near the sense wires, due to the $\vec{E} \times \vec{B}$ effect, the charge drifts at a Lorentz angle ψ ($\psi \approx 32°$ in the case of the ALEPH TPC [8, 9]) towards the wires. The effective spread of the recorded charge projected from the wire onto the pad plane is therefore different for tracks crossing at the left and right sides of a sector. For radial tracks it is proportional to $(\tan\alpha_w - \tan\psi)\cos\alpha_w$ and leads to $\hat{\sigma}^2 \propto (\tan\alpha_w - \tan\psi)^2\cos^2\alpha_w$. This is shown in figure 3c for wire crossing angles up to 30°. $\hat{\sigma}^2$ changes by about 0.025 from one side of an inner sector to the other.

2.2 Pad Response at Sector Edges

The coupling between sense wires and pads changes slightly towards the edges of the sectors. As a consequence the electronics calibration procedure cannot be applied directly for the edge pads. Furthermore the pad response function is locally affected thus distorting the reconstructed coordinates. In order to compensate for the deterioration, the last two pads of a row at the sector edges were built with half the normal width. In figure 4a the fit residuals for high momentum tracks from leptonic Z^0 decays are plotted as a function of $\Delta u = u - u_{\mathrm{hp}}$. Here, u is an azimuthal coordinate close to one sector edge and u_{hp} the azimuthal position of the centre between the two half pads on the same sector edge. $\Delta u < 0$ means that the coordinate is between the sector edge and u_{hp}. Coordinates containing one or two half pads are seen to be systematically shifted towards the inside of the sectors, indicated here by a negative residual.

These distortions are fully corrected by applying an empirical factor of about 1.4 to the pulse heights of half pads. In addition a systematic azimuthal shift is also applied in the rare case of coordinates containing two half pads. The resulting residuals are centred, as can be seen in figure 4b. However, the azimuthal resolution for coordinates with half pads is degraded by 30% to 50%.

3 Single Coordinate Resolutions

For the azimuthal coordinate resolution $\sigma_{r\varphi}$, one expects qualitatively the same dependences on the pad crossing angle α_p, the wire crossing angle α_w and the drift length l_{D} as for the pad response width. In addition, the statistics of the drifting electron cloud has

to be considered. For example this leads to a more complicated dependence of $\sigma_{r\varphi}$ on the drift length, because the drifting charge cloud changes structure as a function of the drift length. A more detailed discussion of the expected contributions to $\sigma_{r\varphi}$ can be found in ref. [1].

The longitudinal resolution σ_z is expected to vary with the dip angle λ of the track. With increasing dip angle the pulses become longer in time, thus decreasing the z measurement accuracy. The additional effect of longitudinal diffusion on pad coordinates is negligible.

Figure 5 shows the azimuthal coordinate resolution for isolated coordinates measured with leptonic Z^0 decays. An overall resolution of $\sigma_{r\varphi} = 173$ μm is measured. All resolutions quoted are corrected for the correlation between the error on the coordinates and the fitted track positions and are therefore larger than the widths of the residual distributions (163 μm for $\sigma_{r\varphi}$). The dependence of $\sigma_{r\varphi}$ on the drift length l_{D} is shown in figure 6. For small drift lengths, the resolution reaches 160 μm. The dependence of $\sigma_{r\varphi}$ on the pad crossing angle α_p, measured with low momentum tracks from hadronic Z^0 decays, is shown in figure 7. For pad crossing angles exceeding a few degrees, this contribution is dominant. The dependence is parameterised with the expression $\sigma^2_{r\varphi} = (0.2\,\mathrm{mm})^2 + (2.3\,\mathrm{mm}\cdot\tan\alpha_p)^2$. The resolution $\sigma_{r\varphi}$ at $\alpha_p = 0$ is slightly worse than that measured in leptonic decays. This degradation is a result of overlapping coordinates in events with high track density, especially for the inner pad rows. A purely geometrical error parameterisation has to be a compromise. No significant dependence of $\sigma_{r\varphi}$ on the wire crossing angle α_w was found for high momentum tracks ($\alpha_p \approx 0$) in the range $-30° < \alpha_w < 30°$. This is expected from measurements [9, 10], which show that the strong influence of α_w gets reduced by transverse diffusion effects for the large drift length (up to 220 cm) for particles produced at the origin of the TPC.

The longitudinal resolution σ_z is shown in figure 8, and its dependence on the dip angle λ of the track is shown in figure 9. A value of $\sigma_z = 740$ μm is achieved for $|\lambda| < 10°$.

The single coordinate resolutions and their functional dependence on α_p, l_{D} and dip angle λ have been measured with events from hadronic and leptonic Z^0 decays. The dependences of the resolution have been parameterised and are used as coordinate errors in the track fit. Figure 10 shows the probability distribution for tracks from hadronic events in a polar angle range of $30° < \theta < 150°$ and with a momentum greater than 0.5 GeV/c for two cases:

- *Not filtered*: Here, all coordinates on the track were used in the track fit. One expects 2% bad coordinates from δ electrons in the gas. This results in a peaking of the distribution at probability 0.

- *Filtered*: Here, all coordinates which were more than 3.9 standard deviations away from the track are removed from the fit. The peaking of the distribution at probability 0 and 1 is due to an overestimation of coordinate errors for isolated tracks and an underestimation of coordinate errors for tracks with many overlapping coordinates in high multiplicity jets. Both extremes are therefore due to compromises in the coordinate error parameterisation. Nevertheless, the overall distribution is flat enough to allow track quality cuts based on the χ^2 of the fit.

4 Laser Calibration

The quality of the track reconstruction depends critically on precise knowledge of systematic distortions of the tracks during their drift towards the end-plates. The ALEPH TPC is therefore equipped with a laser calibration system. It allows the generation of five laser beams on both sides of the TPC at three different azimuthal angles, giving a total of 30 straight ionisation tracks all appearing to originate from the centre of the TPC (see reference [1] for details). It is used to measure and correct residual inhomogeneities of the electric and magnetic fields, which produce systematic displacements of reconstructed coordinates, and also to measure the modulus of the drift velocity of electrons in the TPC gas.

The drift velocity of electrons in the gas as derived from the Langevin equation can be written as a function of electric field, $\vec{E}$, and magnetic field, $\vec{B}$,

$$\vec{v}_{\mathrm{D}} = \frac{\mu}{1+(\omega\tau)^2}\left(\vec{E} + \omega\tau\frac{\vec{E}\times\vec{B}}{|\vec{B}|} + (\omega\tau)^2\frac{\vec{B}(\vec{E}\cdot\vec{B})}{\vec{B}^2}\right), \tag{4}$$

where μ $(= e\tau/m)$ is the electron mobility, ω $(= eB/m)$ is the cyclotron frequency and τ is the mean drift time between two collisions with gas molecules. At small magnetic field (small $\omega\tau$) the first term dominates and the particles drift along the electric field lines; at large magnetic field (large $\omega\tau$) the third term is large, and $\vec{v}_{\mathrm{D}}$ is almost parallel to $\vec{B}$.

In the ideal TPC, $\vec{E}$ and $\vec{B}$ are exactly parallel and (4) simplifies to $\vec{v}_{\mathrm{D}} = \mu\vec{E}$. In reality, however, one expects deviations due to small but finite angles between the fields. These can have two origins:

a) A global angle between $\vec{E}$ and $\vec{B}$ arising from a tilt of the TPC field cage in the magnet.

b) Transverse field components due to inhomogeneities. These are expected to be dominated by the radial components E_r, B_r, since the azimuthal components E_φ, B_φ are constrained by the cylindrical symmetry of the TPC and the magnet.

The field components producing azimuthal coordinate shifts are more important than those producing radial shifts since the momentum resolution is mainly determined by the azimuthal coordinate resolution.

The global angle between electric and magnetic field has been determined from the apparent mismatch of cosmic ray tracks when measured in the TPC or ITC respectively. Using the fact that the $\vec{E}$ field has opposite directions in the two TPC halves the magnitude and azimuthal orientation of the angle was determined from the dependence of the mismatch on the longitudinal position and azimuthal direction of the tracks. The misalignment of $\vec{E}$ and $\vec{B}$ field was found to be 0.03°.

The remaining distortions due to inhomogeneities have to be determined from the magnetic field map, as measured in 1987 [1, 14], and from the straightness of reconstructed laser tracks in the TPC.

4.1 Calibration of Field Distortions Using Laser Beams

Since $\omega\tau$ is large (≈ 9), the most important distortions leading to azimuthal coordinate shifts are produced by B_r, E_τ and B_φ (compare equation 4). The effect of the azimuthal

electric field, E_φ, on azimuthal shifts can be neglected as it is suppressed by a factor $(1+(\omega\tau)^2)^{-1}$. The azimuthal magnetic field can be taken from the field map [1, 14], however, the effect of this correction turns out to be negligible.

The remaining distortions due to B_r and E_r can be measured simultaneously using laser tracks. For this purpose, the laser beams were reconstructed in the rz plane at full and zero magnetic field (using up to 344 z coordinates from the sense wires). From the longitudinal coordinate shifts between full and zero field and the polar angle of the laser beams one can deduce the corresponding radial coordinate shifts $r(B)-r(0)$. Using equation 4 and neglecting the terms $E_\varphi/(\omega\tau)$ and $B_\varphi/(\omega\tau)$, these shifts can be expressed by

$$r(B)-r(0) \;\approx\; \frac{(\omega\tau)^2}{1+(\omega\tau)^2}\int\left(\frac{B_r}{B_z}-\frac{E_r}{E_z}\right)dz \;\equiv\; S_r(B), \tag{5}$$

where the integral runs from the z position of the coordinate to the end-plate. This expression is proportional to the azimuthal coordinate shifts $\Delta_{r\varphi}(B) = S_r(B)/(\omega\tau)$ at full magnetic field due to the field inhomogeneities B_r, E_r. These coordinate shifts can therefore be deduced from the measurement of S_r without the necessity to separate and understand the detailed effects from electric and magnetic field distortions. It requires, however, the knowledge of $\omega\tau$. A precision of 10% for $\omega\tau$ is sufficient for the observed magnitude of field distortions. The measurement of this parameter is described in the next section. An example of the measurement of S_r as a function of the radius from one of the laser beams is shown in figure 11. The precision of this measurement is limited by the reproducibility of the optical steering of the laser beams when changing the magnetic field. In figure 11a the field distortions were artificially enhanced by switching off power supplies to the trim coils at the end of the magnet which are used to correct most of the field inhomogeneities. In this case the field distortions are severe and S_r reaches several millimeters. During normal operation the field is compensated. This leads to much smaller distortions, as shown in figure 11b. The deviations of S_r from 0 would, however, still systematically shift the momentum of 45 GeV/c tracks by +5% for positive particles and -5% for negative particles. The corrections described above are precise enough to eliminate these systematic effects even in the case of figure 11a.

4.2 The Measurement of $\omega\tau$

For the measurement of $\omega\tau$ (see also [15]), a scan over the magnetic field is performed, ranging from -1.5 T to $+1.5$ T, and the r and $r\varphi$ coordinates from the laser tracks are compared for fields of opposite polarity. In analogy to section 4.1 one can derive the quantities $S_r(B)$ and $\Delta_{r\varphi}(B)$ from these measurements:

$$\Delta_{r\varphi}(B) \;\equiv\; \frac{1}{2}\left(r\varphi(+B)-r\varphi(-B)\right) = \frac{\omega\tau}{1+(\omega\tau)^2}\int\left(\frac{B_r}{B_z}-\frac{E_r}{E_z}\right)dz, \tag{6}$$

$$S_r(B) \;\equiv\; \frac{1}{2}\left(r(+B)+r(-B)\right)-r(0) = \omega\tau\,\Delta_{r\varphi}(B). \tag{7}$$

These relations follow from equation 4 without any assumptions on azimuthal field components.

To increase the sensitivity of the measurements of S_r and $\Delta_{r\varphi}$, the trim coils of the magnet were not powered. This enhances the radial magnetic field which directly enters

the integral in equation 6. In principle one can also consider the analogous quantities $S_{r\varphi}(B)$ and $\Delta_r(B)$ which are related by $S_{r\varphi} = -\omega\tau\Delta_r$ and which are proportional to $\int\left(\frac{B_\varphi}{B_z} - \frac{E_\varphi}{E_z}\right) dz$. Experimentally it was found, however, that these quantities are too small to be measured within the systematic errors, showing that the azimuthal field components are at least an order of magnitude smaller than the radial components. This is not surprising since the trim coils affect only B_r but not B_φ, the latter being constrained by the approximate cylindrical symmetry of the magnet.

The limiting systematic effect in this measurement is again the reproducibility of the optical laser steering which changes slightly with varying magnetic field. This is demonstrated in figure 12 where S_r is plotted versus $\Delta_{r\varphi}$ for all measured coordinates and several examples of magnetic fields. The linear dependence between S_r and $\Delta_{r\varphi}$ is clearly visible. The slope $\omega\tau$ increases with magnetic field such that the measurements for $\Delta_{r\varphi}$, which at small fields yield values of several centimeters, become comparable and even smaller than the uncertainties (of several 100 μm) due to the laser steering in the azimuthal direction. The parameter $\omega\tau$ can therefore only be measured at relatively small fields of up to 0.5 T and has to be extrapolated to large fields using $\omega\tau = (eB/m)\tau \propto B$. Even at medium fields it is important to correct all coordinates for visible steering effects.

The results of the fits for $\omega\tau$ as a function of B are shown in figure 13. The error bars are almost entirely of systematic origin and are strongly correlated. A global straight-line fit (which takes all correlations between data points into account) yields $\omega\tau/B = (5.9 \pm 0.2)\ \mathrm{T}^{-1}$ with $\chi^2 = 7.5$ for 8 degrees of freedom, which is shown in figure 13. The operating field of $B = 1.5$ T for the ALEPH detector hence corresponds to $\omega\tau = 8.9 \pm 0.3$.

4.3 Drift Velocity

The measurement of the drift velocity by the laser system employs the fact that in a TPC the radial dependence of the drift time dt/dr and the polar angle θ of a track are related via $dt/dr \cong -1/(v_\mathrm{D} \cdot \tan\theta)$. Taking drift time differences with respect to a fixed reference beam in each azimuthal plane, systematic effects of electronic delays and sector alignment cancel. The main component v_z of the drift velocity is then determined via the equation

$$v_z \cdot \frac{d(t_1 - t_2)}{dr} = \frac{1}{\tan\theta_2} - \frac{1}{\tan\theta_1} - p_\varphi \cdot \left(\frac{1}{\sin^2\theta_2} - \frac{1}{\sin^2\theta_1}\right) , \qquad (8)$$

where $t_{1,2}$ are the measured drift times of two laser beams as obtained from the sense wires, $\theta_{1,2}$ are the well known (to $\pm 0.02°$) deflection angles [13] of the mirrors that direct the beams into the chamber and p_φ is a free parameter for each azimuthal plane taking into account the combined effect of radial drift velocity components and the optical steering of the beam in that plane. Using 100 laser shots, one obtains a statistical precision in v_z of 0.02% and a systematic uncertainty of 0.1%.

Figure 14 displays results from a scan of the drift velocity as function of the applied electric field. A clear maximum is observed and is used as the working point for standard operation. Figure 15 displays the long-term evolution of the drift velocity in the TPC. Initially, v_D was observed to be very stable (to $\approx 0.05\%$) yielding identical values before and after the shut-down in the first months of 1990. In June 1990 v_D dropped by about 1%, after repair work for which the TPC had to be opened. In the following weeks, v_D slowly approached the old long-term average. This sudden jump in v_D is believed to be due to slight changes in the composition of impurities in the gas which are unavoidable

when opening the chamber. The continuous monitoring of v_D was therefore a necessary requirement for reliable performance of the TPC during the whole running period.

5 Alignment of TPC Sectors

The position of each wire chamber in the TPC end-plate is mechanically determined by pins located with high precision on the end-plate frame. The positions of these sectors were determined in two independent optical survey measurements to an accuracy of about 100 μm [11]. The position in the $r\varphi$ plane of the pads relative to the reference points of the sector is known by construction with a precision of the order of 60 μm. This error is smaller than the measurement error on the position of the reference points.

The relative alignment of the 18 sectors in each end-plate has also been determined with two track events from the process $e^+e^- \rightarrow \mu^+\mu^-$, where the radially outgoing muons have a momentum equal to the beam energy. Here, only tracks from events with two identified muons and an acollinearity angle of less than 0.3° between the two muons were used. Each muon track was fitted with three helix segments, one measured by the ITC [1], one measured in an inner sector and one in an outer sector of the TPC. The track fit was made with a common radius of curvature and dip angle for all three helix pieces, but allowing for offsets in the azimuthal plane at the boundaries between ITC and TPC and between inner and outer TPC sectors. The radial and azimuthal positions of each sector and its rotation about its centre were determined by minimising the azimuthal deviations between the TPC and ITC helix pieces. In this way, the sectors in each TPC end-plate were aligned relative to each other and the complete end-plate was aligned globally to the ITC. As a consequence, the two TPC end-plates are also aligned relative to each other. A Monte Carlo simulation of $e^+e^- \rightarrow \mu^+\mu^-$ events, where the sectors of the TPC were deliberately misaligned to each other, showed that with this procedure and a sample of about 5000 dimuon events one reaches an accuracy on the sector alignment parameters which is superior to the survey measurements.

Figure 16 shows the mean azimuthal fit residuals as a function of pad row radius before and after the alignment corrections. For this example, tracks were fit in an inner sector and extrapolated to an adjacent outer sector. The discontinuity at the transition from inner to outer sector (pad row 9 to 10) is removed by the alignment corrections.

6 Momentum and Impact Parameter Resolutions

Figure 17 shows the ratio of the beam energy over the momentum measured in the TPC for tracks from $Z^0 \rightarrow \mu^+\mu^-$ decays. A track was required to have 21 TPC coordinates, and the acollinearity angle between the positive and the negative muon was required to be smaller than 0.3° in order to eliminate radiative events. These events were also removed by requiring the sum of the energies of all clusters in the electromagnetic calorimeter which were not associated with the two muons to be less than 100 MeV.

A momentum resolution of

$$\Delta p/p^2 = 1.2 \cdot 10^{-3} \left(\frac{\mathrm{GeV}}{\mathrm{c}}\right)^{-1} \tag{9}$$

for the TPC is achieved, in agreement with its design specification [12]. Together with

the ITC, the momentum resolution is

$$\Delta p/p^2 = 0.8 \cdot 10^{-3} \left(\frac{\mathrm{GeV}}{\mathrm{c}}\right)^{-1} . \tag{10}$$

The ratio of the beam energy over the momentum measured by the ITC/TPC tracking system for dimuon events is shown separately for positive and negative muons in figure 18 before and after applying the field and alignment corrections described in previous sections. One sees that the corrections centre both distributions and reduce their widths.

Knowledge of the resolution and systematic effects in the determination of track impact parameters is vital for analysing decays of long-lived hadrons or leptons producing secondary vertices in their decays. Therefore the impact parameters d_0 of the two muons produced in the leptonic decays $Z^0 \rightarrow \mu^+\mu^-$ were studied, where d_0 is defined as the signed distance of closest approach of a track to the beam axis, with the sign equal to that of the angular momentum of the track with respect to this axis. The sum Σd_0 of the d_0 parameters of the positive and negative muon is independent of the beam position and vanishes on average. Any systematic offset indicates residual track distortions, which can bias the measurement of secondary vertices. Figure 19 shows the distribution of Σd_0 for muons measured by the TPC alone. The mean value of (-4 ± 13) μm is compatible with 0. The distribution has a relatively large width of 438 μm. This is due to the extrapolation of the track fit with a finite momentum error from the innermost TPC coordinate at a radius of 39.9 cm to the track origin. The impact parameter resolution of the ALEPH tracking system is, however, not determined by the TPC, but mainly by the inner tracking detectors close to the vertex. Using the ITC/TPC system, the Σd_0 distribution is found to be still centred (mean = (0 ± 6) μm) but to have a significantly improved width of 185 μm, corresponding to an impact parameter resolution $\sigma_{\mathrm{track}} = \sigma_{\Sigma d_0}/\sqrt{2} = 131$ μm.

The performance of the tracking system can also be judged from the invariant mass distribution of $\pi^+\pi^-$ pairs originating from secondary vertices in hadronic Z^0 events. The K^0 peak in figure 20 has a full width at half maximum of 9.5 MeV/c^2.

7 Two Track Resolution

By comparing pairs of tracks from particles with the same and opposite charge as a function of the opening angle α of the pair, the two-track resolving capabilities of the chamber were studied. While pairs of oppositely charged tracks bend apart in the magnetic field, pairs of particles with the same charge stay closer together and therefore have a higher probability for coordinate confusion.

Figure 21 displays the distribution of reconstructed pairs $dN/d\alpha^2$ as function of α, starting with $\alpha \geq 0.1°$ to avoid large fluctuations below 0.1°. The distributions for same and oppositely charged pairs of particles are normalised to each other in the interval $5° \leq \alpha \leq 10°$. Only tracks coming from the interaction vertex and traversing all 21 pad rows were taken. Both tracks of a pair had to have a momentum larger than 5 GeV/c and at least four separate coordinates on common pad rows. This separation is better at outer radii. From a Monte Carlo simulation of hadronic Z^0 decays one finds a constant reconstruction efficiency for track pairs in the normalisation interval $5° \leq \alpha \leq 10°$ of (95.7 ± 1.1)%, which is consistent with the single-track finding efficiency of 98.6% for particles with momenta greater than 1 GeV/c in jets at $\sqrt{s} = 91$ GeV (the efficiency for

isolated tracks which cross all 21 pad rows is practically 100%). This shows that in the normalisation interval track pairs are fully resolved.

From the depletion of $dN/d\alpha^2$ of same sign charged particle pairs one deduces that at an opening angle of less than 2° neighbouring tracks with momenta greater than 5 GeV/c are no longer properly resolved. However, the present pattern recognition is not yet exploited to the ultimate limit.

It has been verified by Monte Carlo simulation that the depletion in the distribution of track pairs with same sign charge is not a consequence of pure short-range charge correlations within jets but is dominated by tracking effects.

8 dE/dx Calibration and Resolution

In addition to its principle role as a tracking device, the TPC also serves to separate particle species according to measurements of their specific energy loss by ionisation, $\mathrm{d}E/\mathrm{d}x$. This is important, when used in conjunction with the electromagnetic calorimeter, for identification of electrons in hadronic events [16] and also provides some ability to distinguish pions from kaons or protons. The $\mathrm{d}E/\mathrm{d}x$ is measured from the sense wire pulses, of which there are at most 344 for a track traversing the full radius of the TPC. The offline reconstruction uses for the $\mathrm{d}E/\mathrm{d}x$ analysis only those wire pulses which match in z with a *single* track.

The $\mathrm{d}E/\mathrm{d}x$ of a track is defined to be the mean of the 60% of its associated wire pulses, or $\mathrm{d}E/\mathrm{d}x$ samples, with the lowest pulse heights (60% truncated mean), after applying corrections for variations of sample length and for attenuation of the charge with drift. The attenuation has been measured using an auxiliary wire chamber positioned in the same gas flow as the TPC and is found to be only 1.2% per metre [3], which is negligible compared with the statistical resolution of the $\mathrm{d}E/\mathrm{d}x$ measurement. Due to the large angular acceptance of the TPC, the sample length varies with polar angle by up to a factor of three. This results in a logarithmic variation of the truncated mean, which has been fit using Bhabha and muon pairs to the form

$$\frac{\mathrm{d}E}{\mathrm{d}x} \propto \frac{1}{1 + C \ln(\Delta x/\Delta r)}, \tag{11}$$

where $\Delta r = 0.4\,\mathrm{cm}$ is the distance between sense wires and Δx is the corresponding track length. The fit value of C is 0.172.

The r.m.s. variation of gain within each of the 36 TPC sectors was kept to less than 3% by appropriate manufacturing tolerances [1], but the gain variations from sector to sector must be calibrated from the LEP data. This is done by normalising the measurements such that the average $\mathrm{d}E/\mathrm{d}x$ of hadrons in the relativistic-rise region is the same in all sectors. The r.m.s. variation in gain over the 36 sectors is about 3% and is found to be stable with time, with the exception of occasional shifts, most of which can be related to known changes in the TPC hardware.

Since the TPC operates at atmospheric pressure, the effective gain changes from run to run. It is calibrated from data using minimum-ionising pions in the momentum range from 0.3 GeV/c to 0.6 GeV/c, where there is a large separation between the $\mathrm{d}E/\mathrm{d}x$ of pions and that of all other particle types (except muons, which are rare and give $\mathrm{d}E/\mathrm{d}x$ close to that of pions). The data are grouped into blocks of runs such that the pressure variation within a block is negligible, and the position of the pion peak is measured for

each block. The dE/dx for each block is thereby normalised such that minimum-ionising particles have $\langle dE/dx \rangle \equiv 1$.

The sample of minimum-ionising pions also is used to determine the dE/dx resolution in hadronic events. The resolution as a function of the number of dE/dx samples, N, is fit to the form

$$\sigma_I/I = \sqrt{\sigma_a^2/N + \sigma_b^2}\,, \tag{12}$$

$I \equiv \langle dE/dx \rangle$, from which we find $\sigma_a = 0.834$ and $\sigma_b = 0.019$. Note that the constant term σ_b of almost 2% gives a significant contribution to the resolution. The sample of pions is in a momentum range where the track curvature is large (particles with transverse momentum less than about 0.4 GeV/c loop in the TPC), so the resolution must be checked with tracks of higher momentum. This can be done in hadronic events by using electron candidates identified by the electromagnetic calorimeter. There is a substantial background in this sample, but it can be reliably subtracted by using the dE/dx spectrum of tracks which are *not* identified as electrons [16]. A fit to the resolution of the electrons versus number of samples prefers $\sigma_b = 0$ and $\sigma_a = 0.835$, indicating a resolution of 4.6% for electrons in hadronic events with the full complement of wires. The resolution is slightly better for low multiplicity events. In dilepton events, with pairs of electrons or muons at $p = 45\,\mathrm{GeV/c}$, we find a resolution of 4.4%.

The dependence of the mean dE/dx on particle velocity has been measured from data using a variety of event types. Minimum-ionising pions fix the minimum of the curve, protons are used to fit the low momentum $1/\beta^2$ region, Bhabha events give the plateau position, and dimuons and muons from tau decay give points only slightly below the plateau. The mean dE/dx of pions in the relativistic rise region is determined from fits to dE/dx measurements in multi-hadron events. Each momentum bin is fit to a sum of four Gaussian contributions, for electrons, pions, kaons and protons, with only the position of the pion peak and the normalisations of the four contributions allowed to vary. The results of the fits for the position of the pion peak are then combined with the points from protons, minimum-ionising pions, and dileptons in a fit of a modified Bethe-Bloch formula with six free parameters. This procedure is iterated several times, the improved parameterisation being used in each iteration to fix the positions of the kaon and proton contributions. The resulting parameterisation is shown plotted over a scatterplot of measured dE/dx versus momentum for each of the five particle types (e, μ, π, K, p) in figure 22. The height of the plateau relative to minimum ionising is 1.57.

9 Conclusions

In the first year of LEP running, the ALEPH TPC has proved to be a powerful tracking device with a performance close to the design specifications. Detailed corrections for imaging distortions, based on magnetic field maps and the laser calibration system were applied. All basic chamber parameters and the internal geometric alignment were measured and monitored with tracks from Z^0 decays and/or straight ionisation tracks produced by lasers.

In particular, the ALEPH TPC reaches an azimuthal coordinate resolution of 173μm, a longitudinal resolution of 740μm, a momentum resolution of $\Delta p/p^2 = 1.2 \cdot 10^{-3}$ $(\mathrm{GeV/c})^{-1}$ ($0.8 \cdot 10^{-3}$ $(\mathrm{GeV/c})^{-1}$ together with the ITC), an impact parameter resolution of 131 μm

(together with the ITC) and a dE/dx-resolution of 4.4%. Two equally charged high-momentum particles are fully resolved for opening angles larger than 2°.

10 Acknowledgements

We would like to express our great appreciation to the technical staff in our institutions for their continuous and devoted efforts in constructing this detector. Furthermore, we would like to thank our many colleagues in ALEPH for their continuing and fruitful collaboration.

References

[1] The ALEPH Handbook, *ALEPH 89-77* (1989);
D. Decamp et al. (ALEPH Collaboration), *Nucl. Instr. and Meth.* A**294** (1990) 121.

[2] D. R. Nygren, *PEP* **198** (1975).

[3] T. Barczewski et al., *Nucl. Instr. and Meth.*, A**289** (1990) 176.

[4] B. Lofstedt et al., Time Projection Digitiser, *CERN-EP* F6821-5A4.

[5] S. R. Amendolia et al., *IEEE Trans. Nucl. Sci.*, NS**37** (1990) 1210-1215.

[6] S. R. Amendolia et al., *Nucl. Instr. and Meth.*, A**239** (1985) 192-196;
S. R. Amendolia et al., *Nucl. Instr. and Meth.*, A**252** (1986) 403-406.

[7] W.A. Wenzel, *TPC-LBL-78-14* (1978);
D.L. Fancher, A.C. Schaffer, *LBL-8327* (1978);
D.L. Fancher, A.C. Schaffer, *IEEE Trans. Nucl. Sci.* NS**26** (1979) 150.

[8] S.R. Amendolia et al., *Nucl. Instr. and Meth.* A**217** (1983) 317.

[9] W. Blum et al., *Nucl. Instr. and Meth.* A**252** (1986) 407.

[10] S. R. Amendolia et al., *Nucl. Instr. and Meth.* A**252** (1986) 392.

[11] E. Milotti, ALEPH Internal Note 87-63, 1987;
L. Rolandi, ALEPH Internal Note 89-147, 1989.

[12] ALEPH Collaboration, *Technical Report, CERN/LEPC/83-2* (1983).

[13] ALEPH Internal Note 89-133, 1989.

[14] L.A.T. Bauerdick, Ph.D.-Thesis, Mainz (1990), unpublished.

[15] S. R. Amendolia et al., *Nucl. Instr. and Meth.*, A**235** (1985) 296.

[16] D. Decamp et al. (ALEPH Collaboration), Phys. Lett. B**244** (1990) 551.

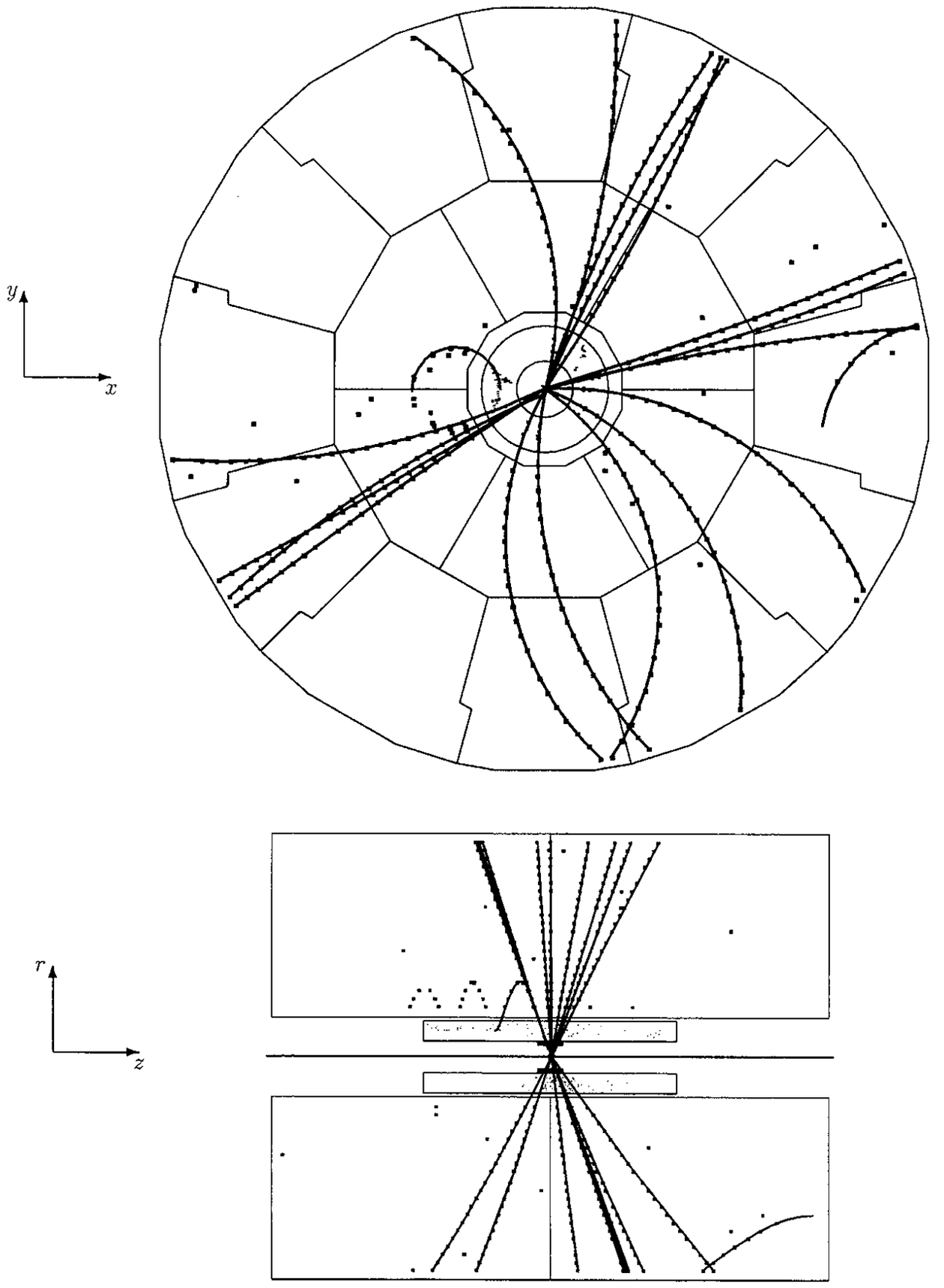

Figure 1: *$r\varphi$- and (downscaled) rz-view of the decay of a Z^0 into hadrons as reconstructed in the ALEPH TPC and ITC.*

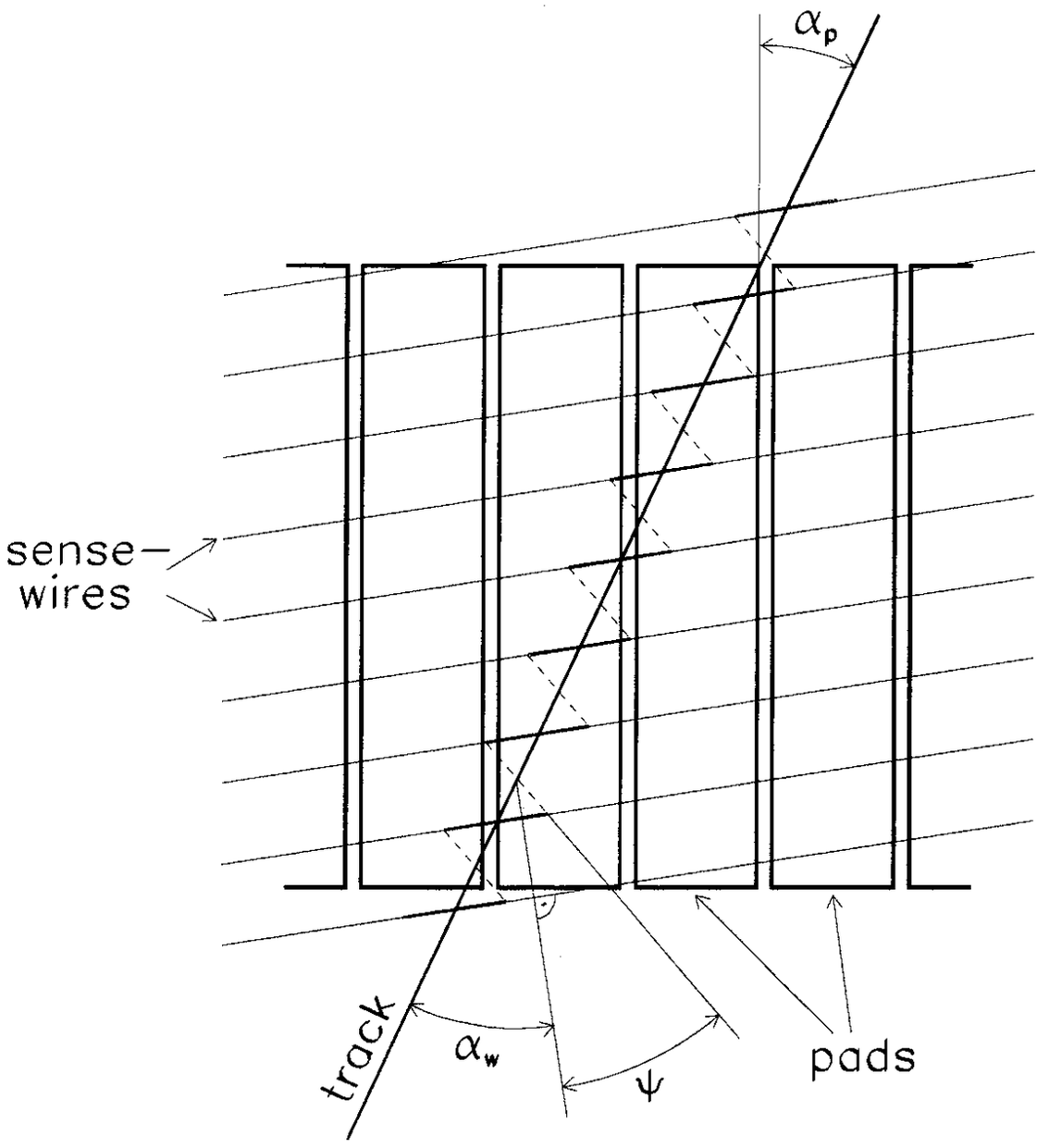

Figure 2: *Definition of angles between track, wire and pad.*

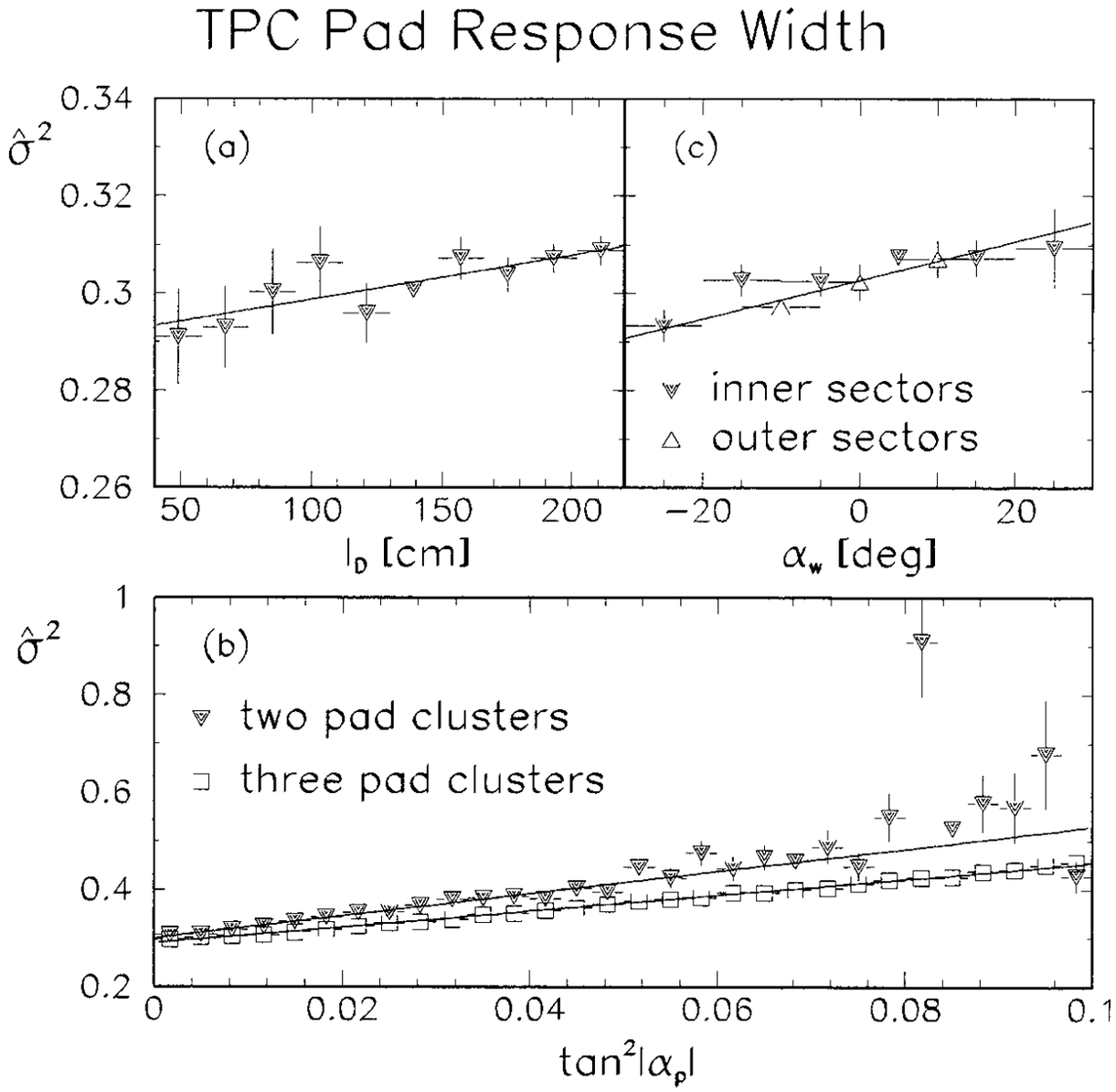

Figure 3: *Pad response width $\hat{\sigma}^2$ as function of (a) drift length for $|\alpha_p| < 0.02\,mrad$, (b) $\tan^2|\alpha_p|$, (c) α_w for $|\alpha_p| < 0.02\,mrad$. The lines show the parameterisations.*

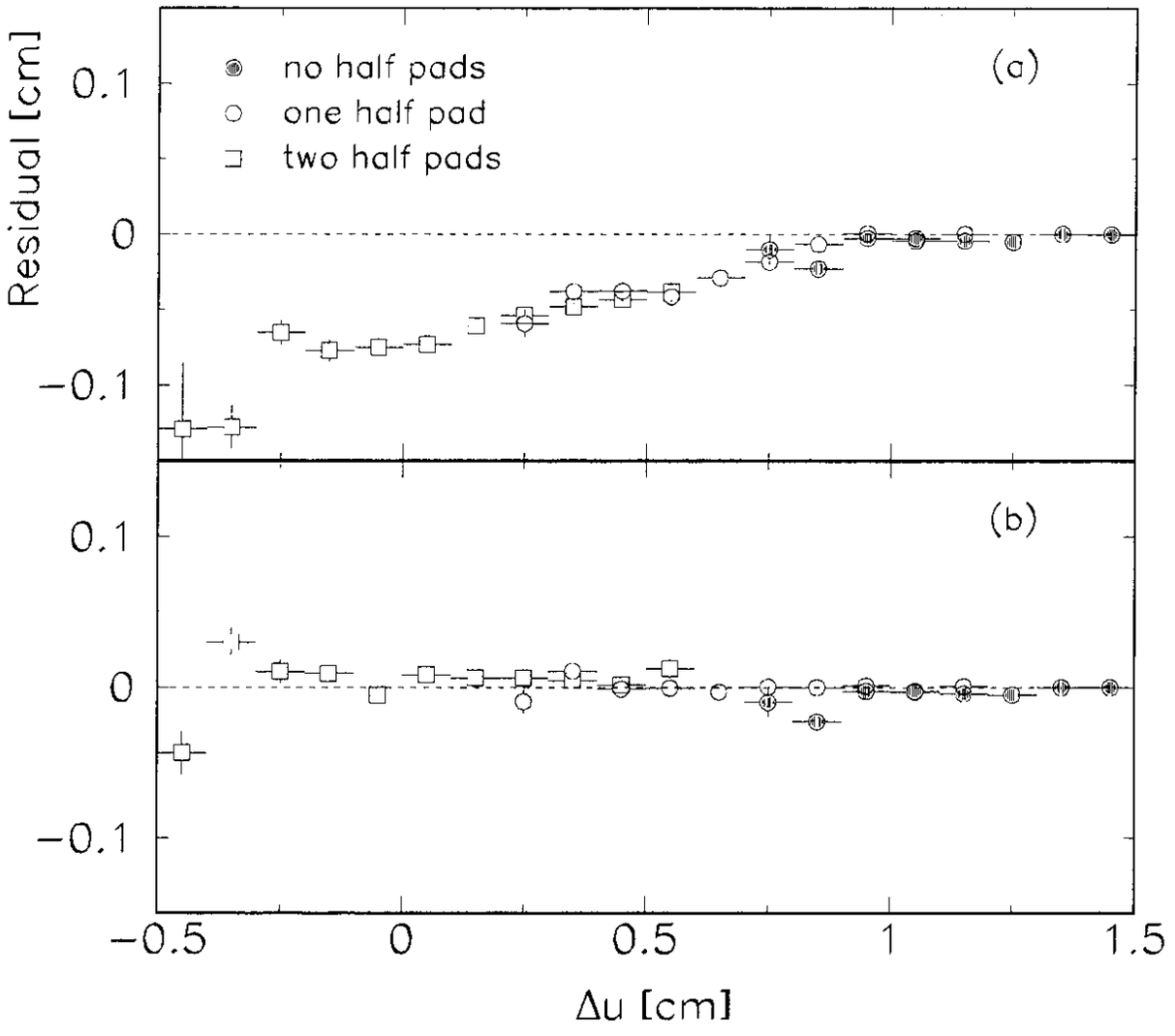

Figure 4: *Residual as a function of Δu. Displayed are the residuals before (a) and after (b) the empirical correction of coordinates containing half pads.*

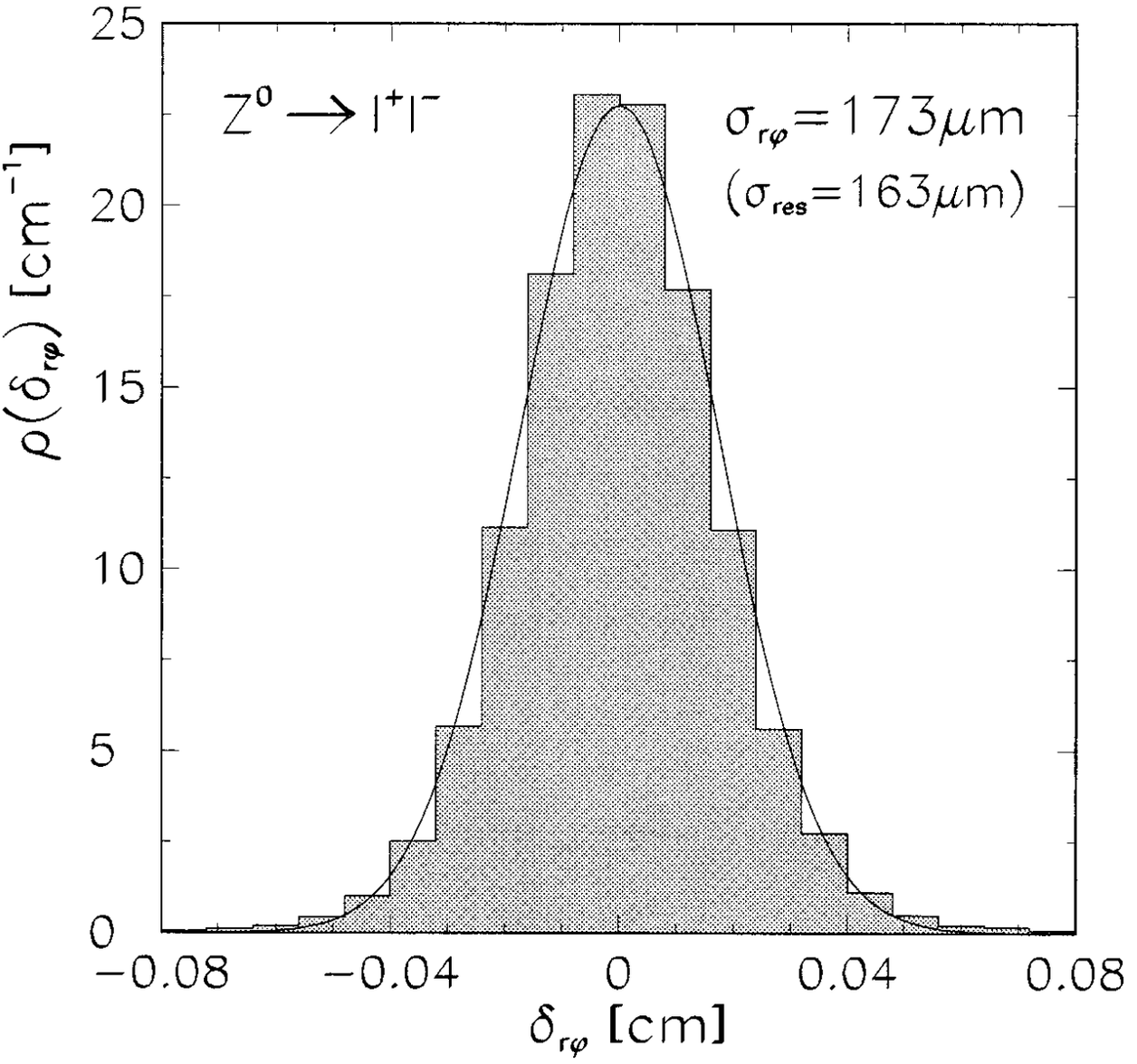

Figure 5: *Azimuthal coordinate resolution, measured with tracks from leptonic* Z^0 *decays.*

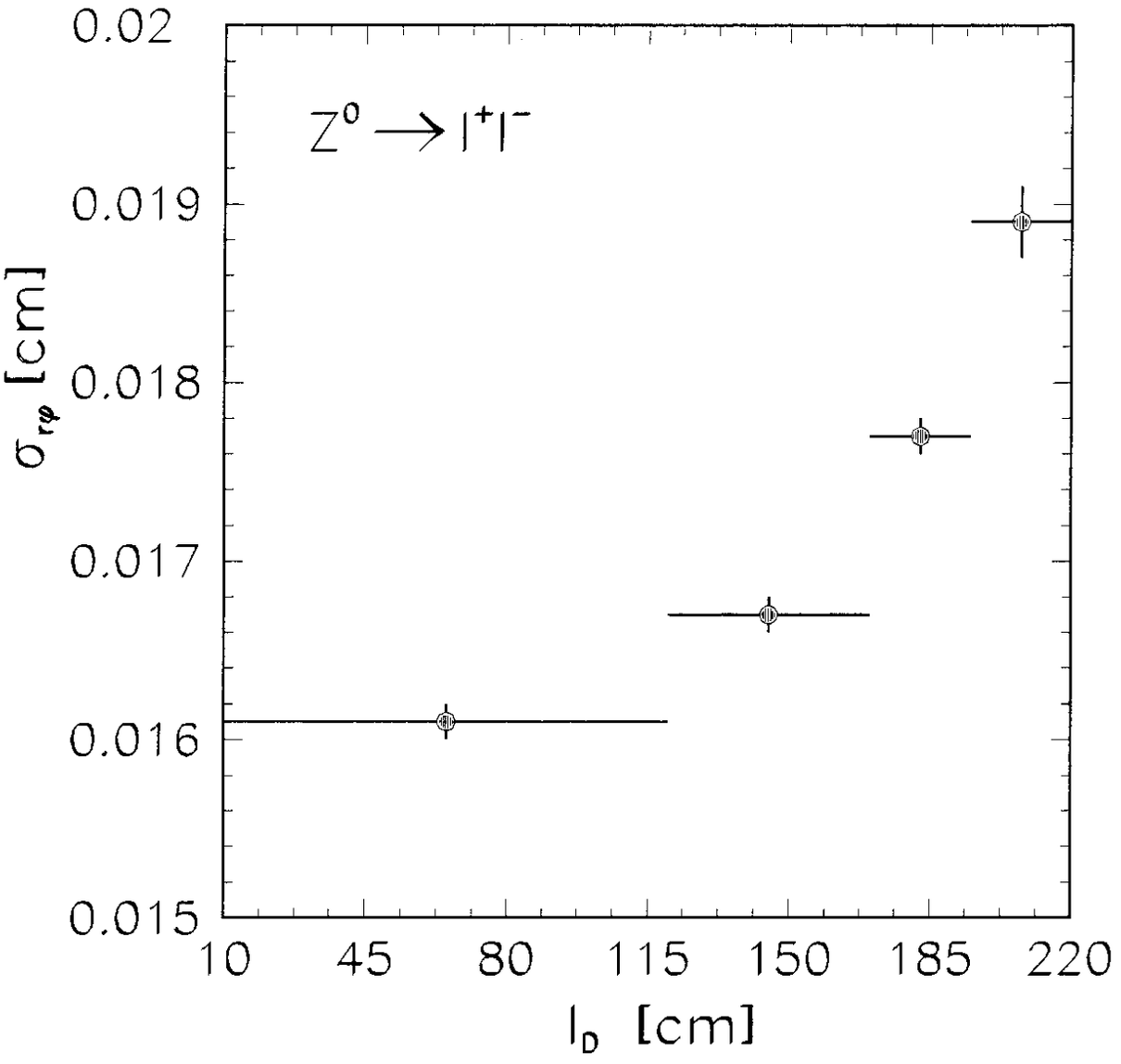

Figure 6: *Dependence of the azimuthal coordinate resolution on the drift length measured with tracks from leptonic Z^0 decays.*

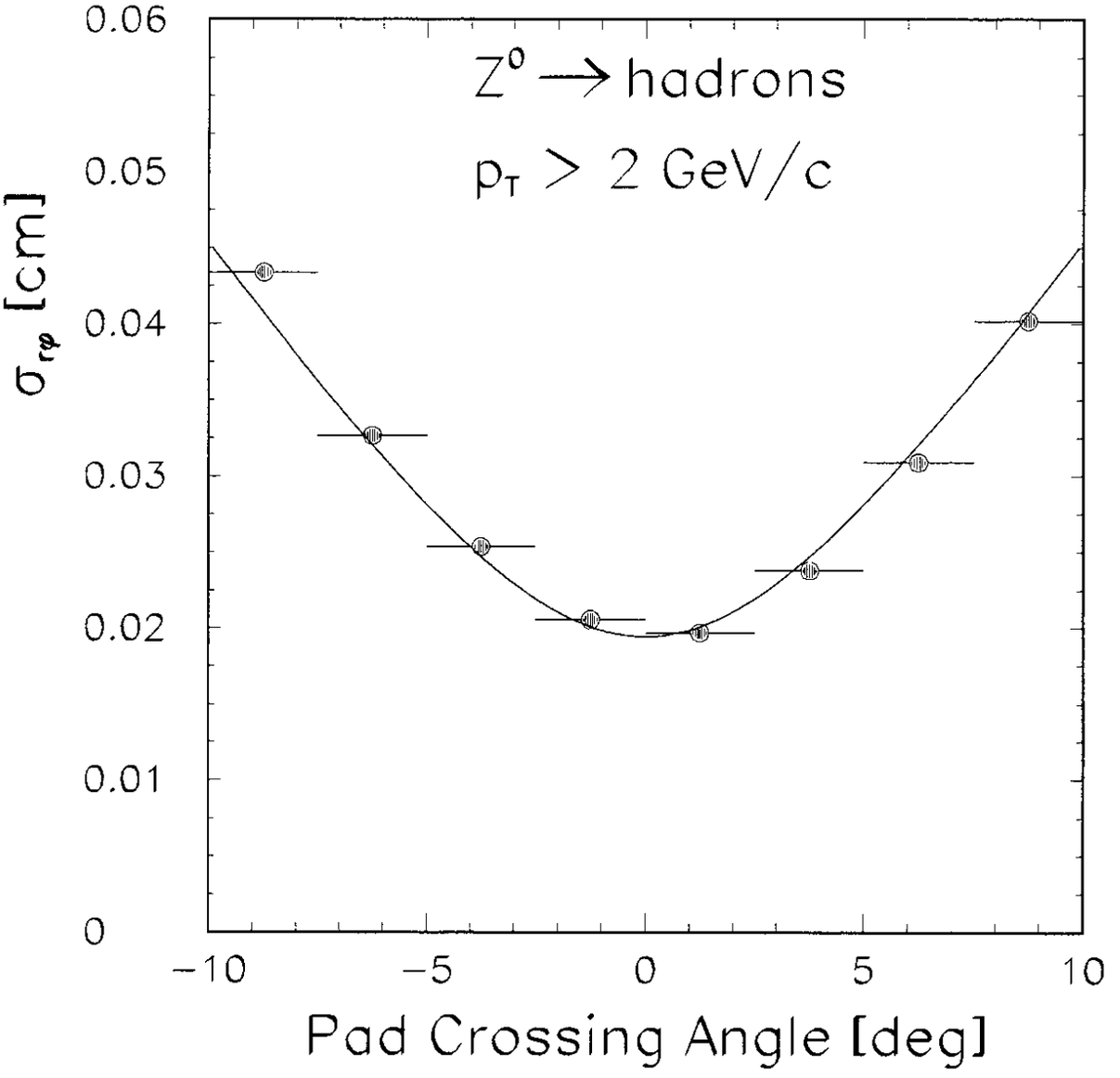

Figure 7: *Dependence of the azimuthal coordinate resolution on the pad crossing angle α_p measured with tracks from hadronic Z^0 decays.*

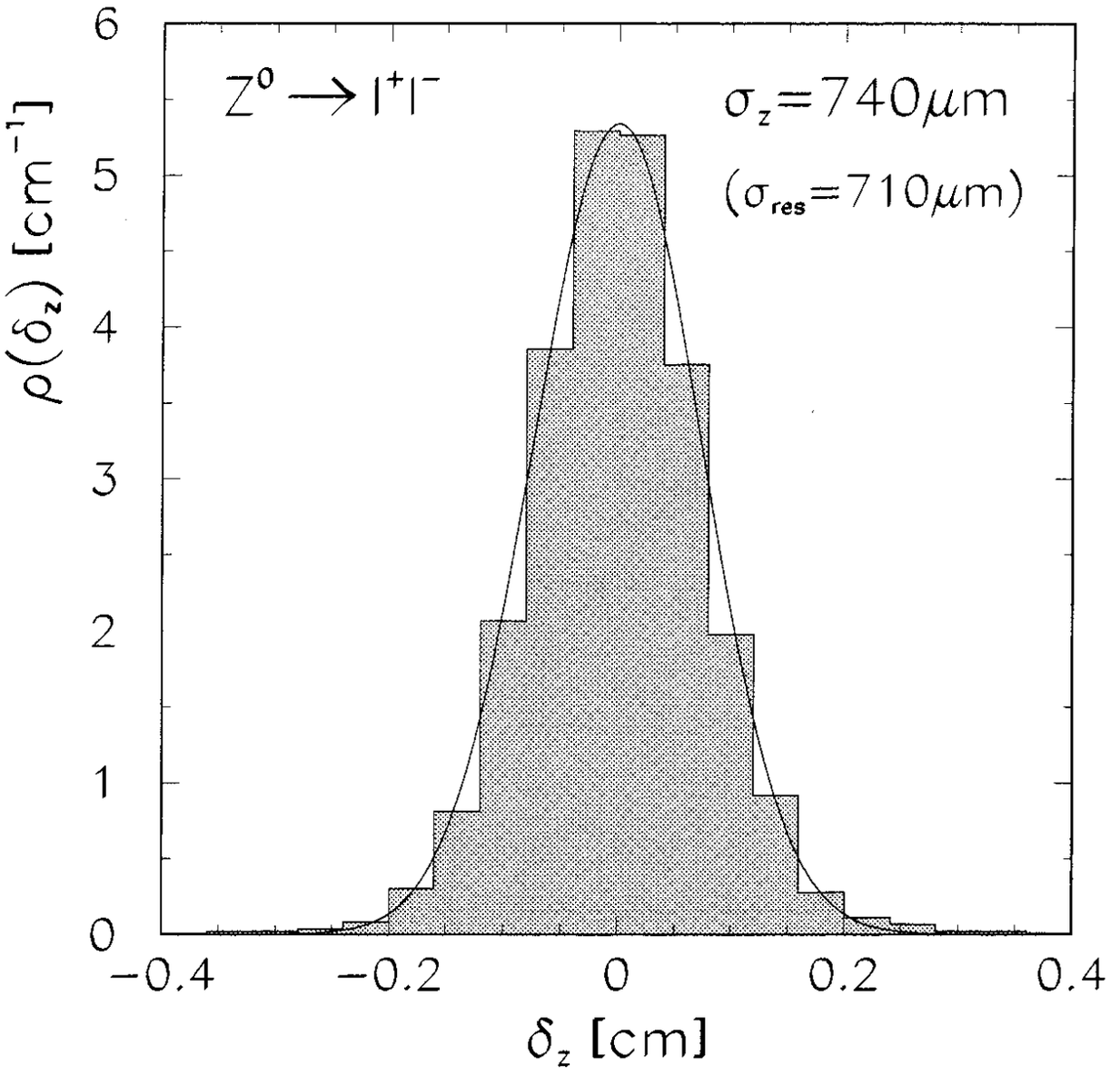

Figure 8: *Longitudinal coordinate resolution, measured with tracks from leptonic* Z^0 *decays.*

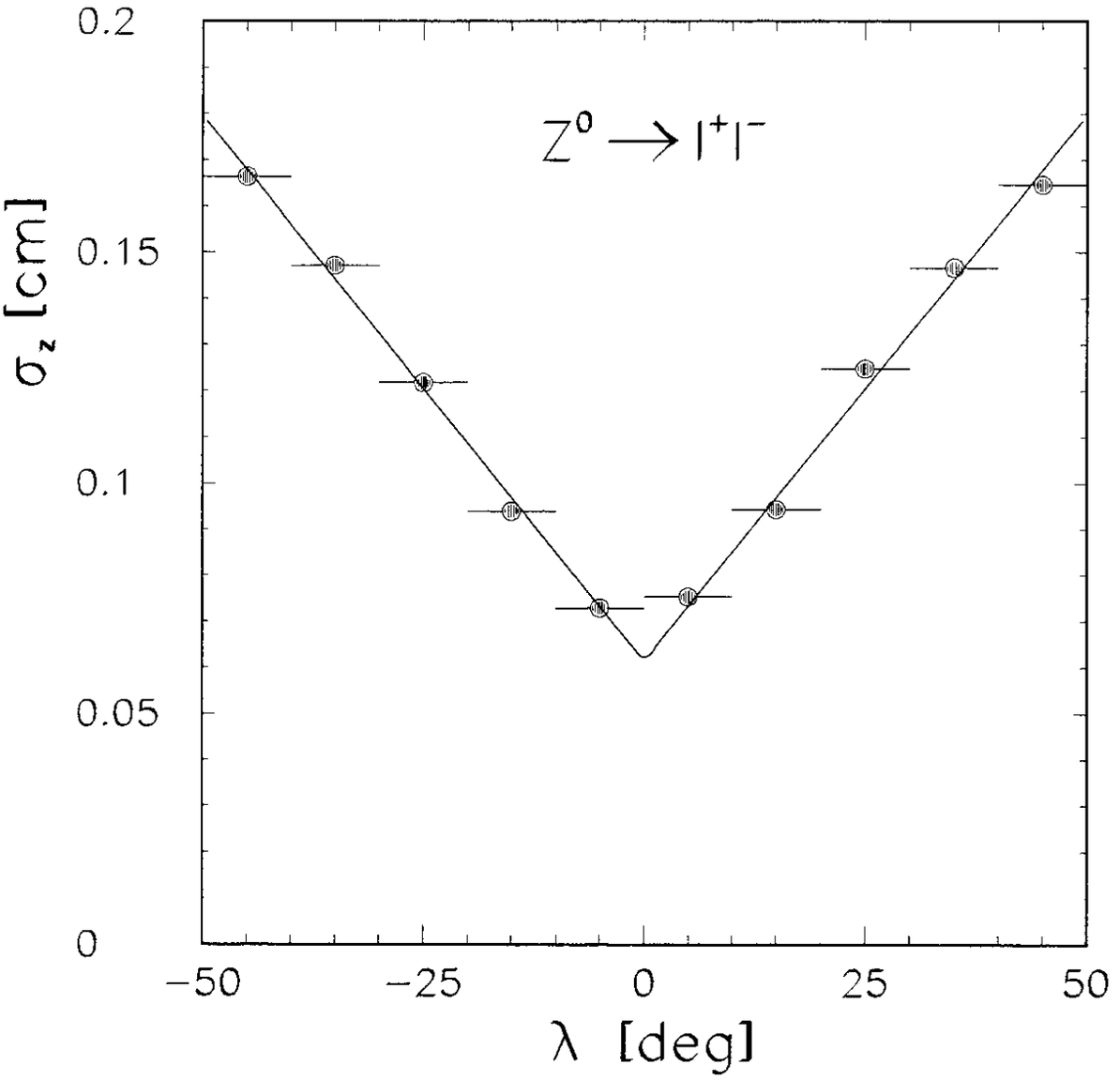

Figure 9: *Dependence of the longitudinal coordinate resolution on the dip angle λ measured with tracks from leptonic Z^0 decays.*

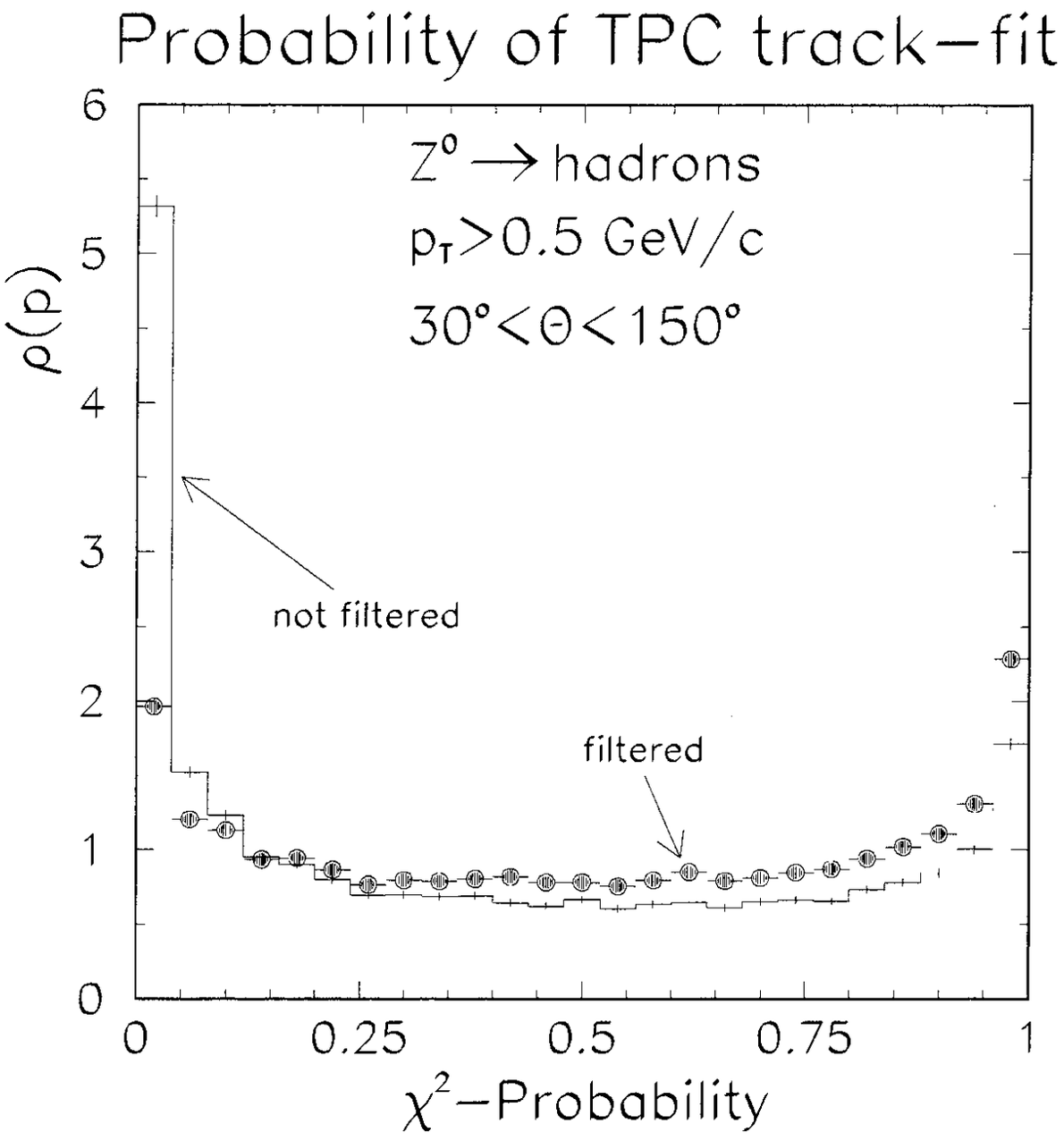

Figure 10: *Distribution of fit probabilities for tracks in hadronic* Z^0 *decays.*

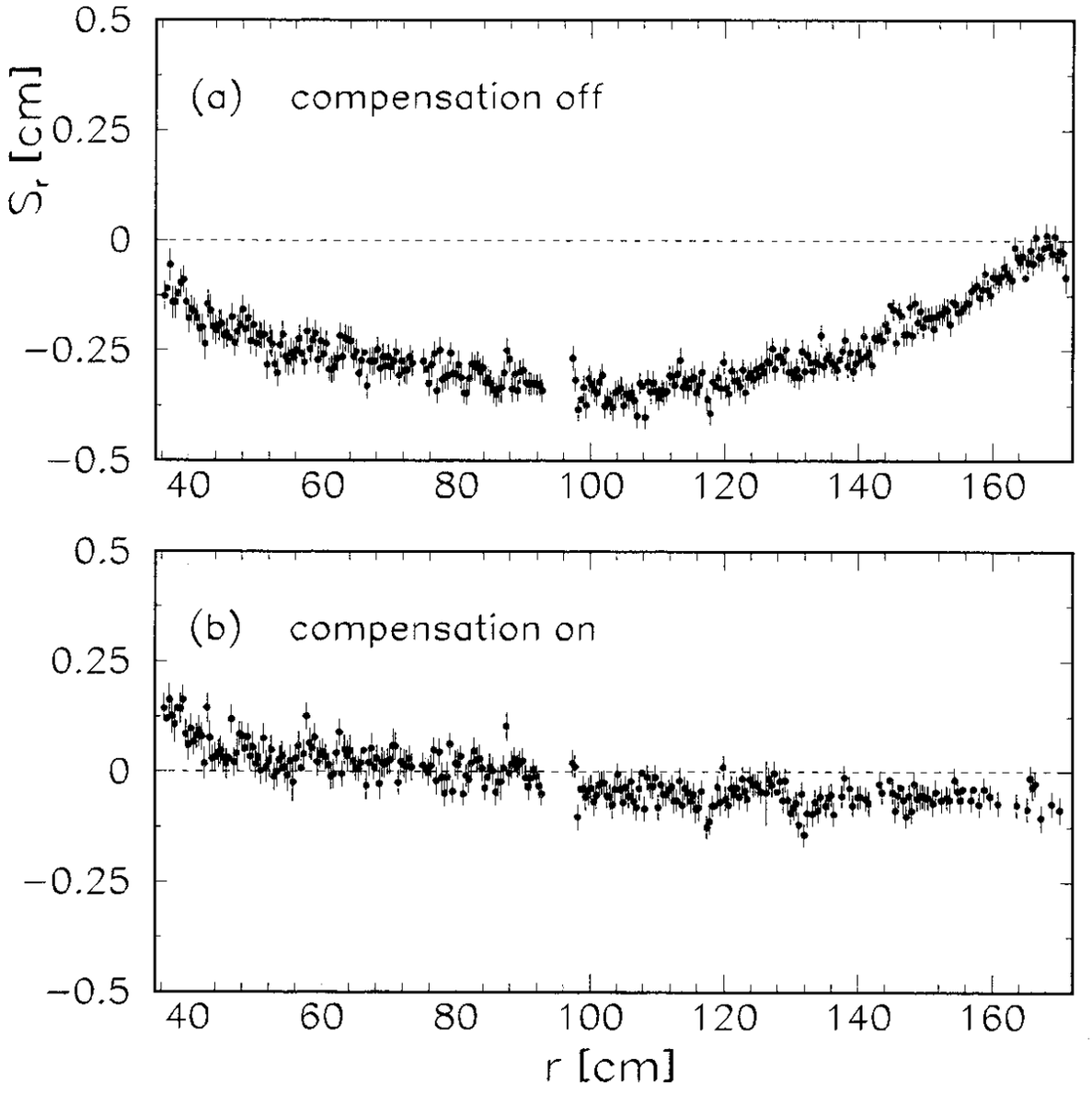

Figure 11: *Radial coordinate displacements between full and zero magnetic field.*

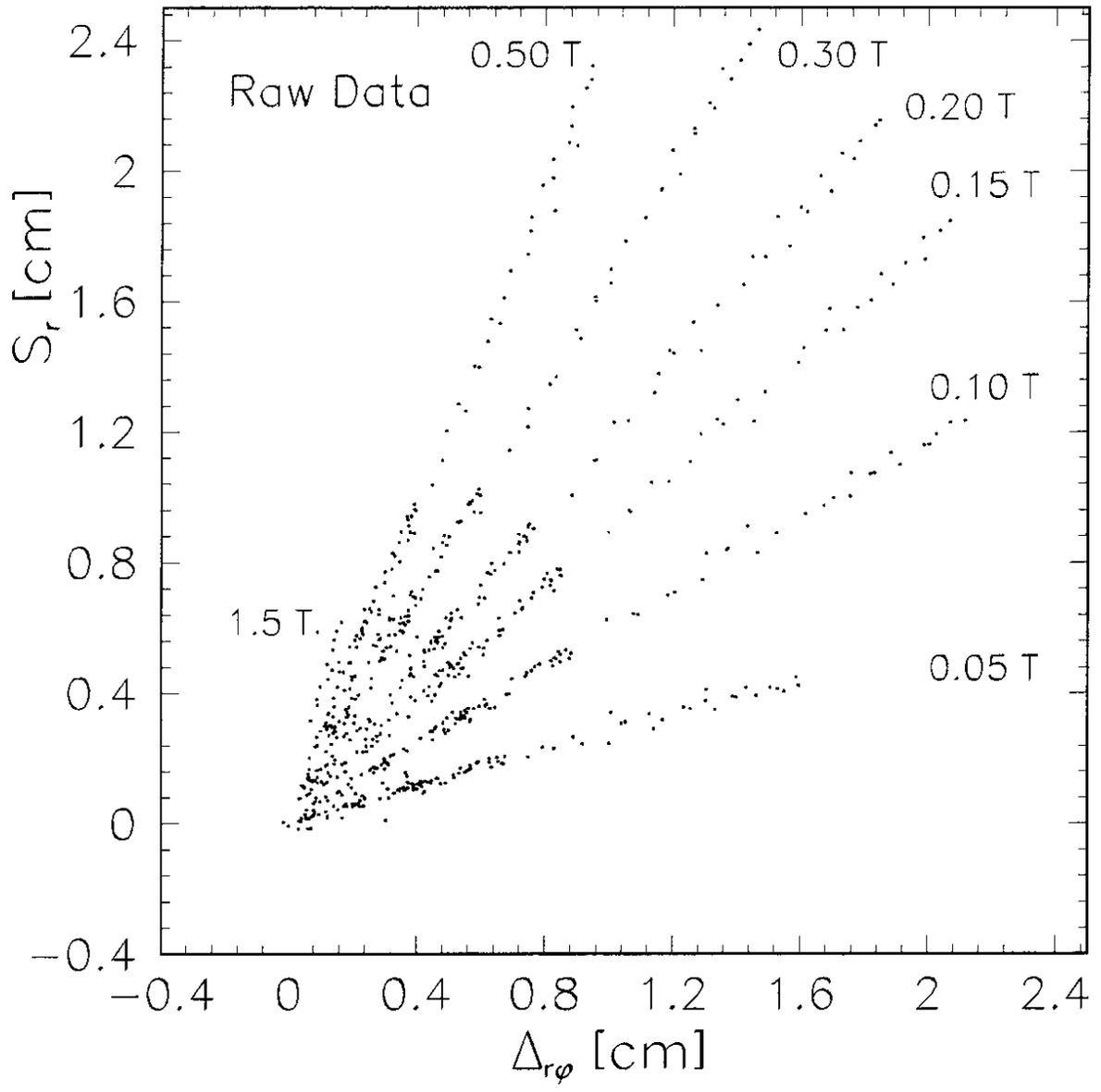

Figure 12: *Uncorrected measurements for $\Delta_{r\varphi}$ and S_r.*

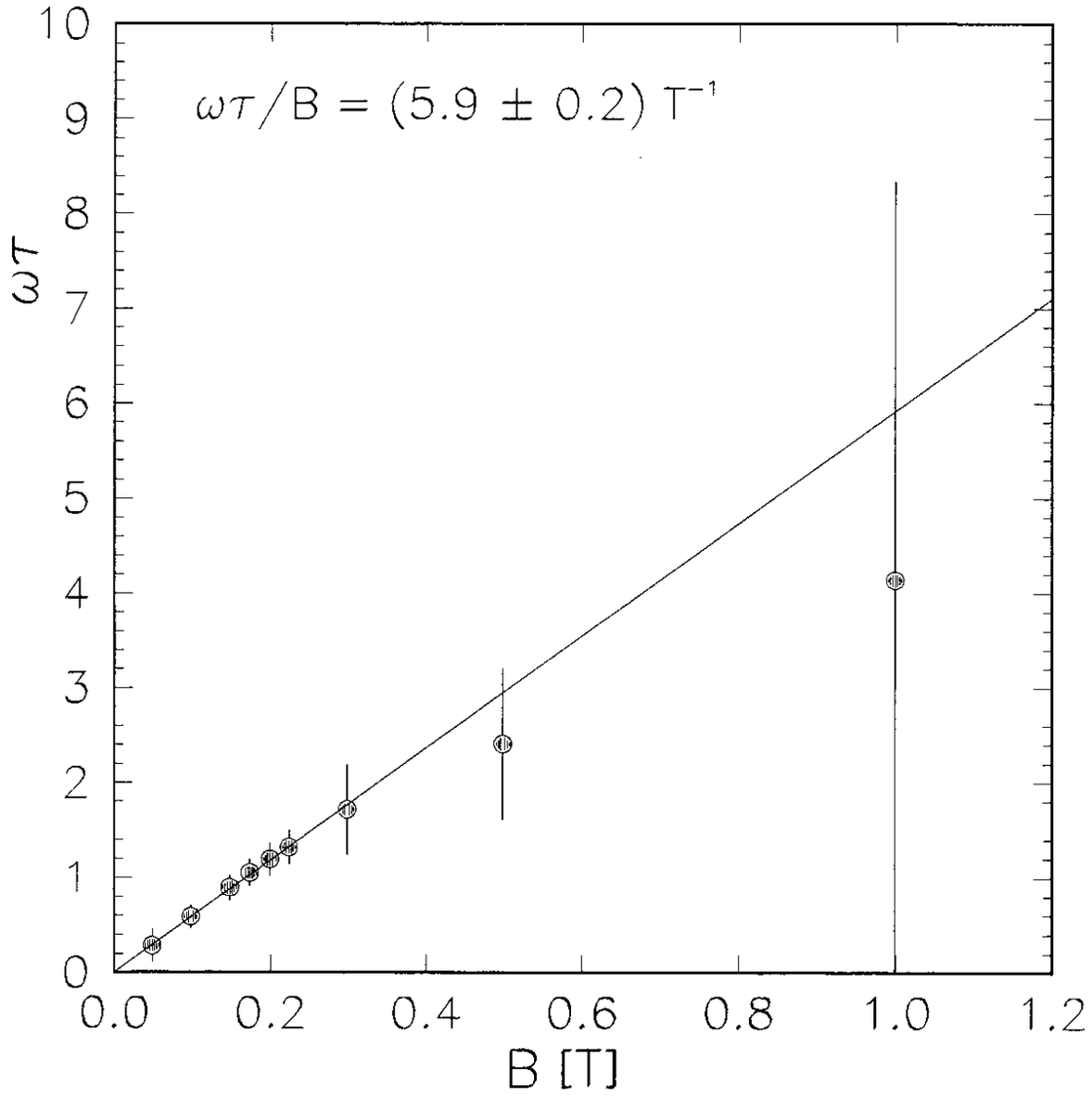

Figure 13: *Results of the fits for $\omega\tau$ as function of B.*

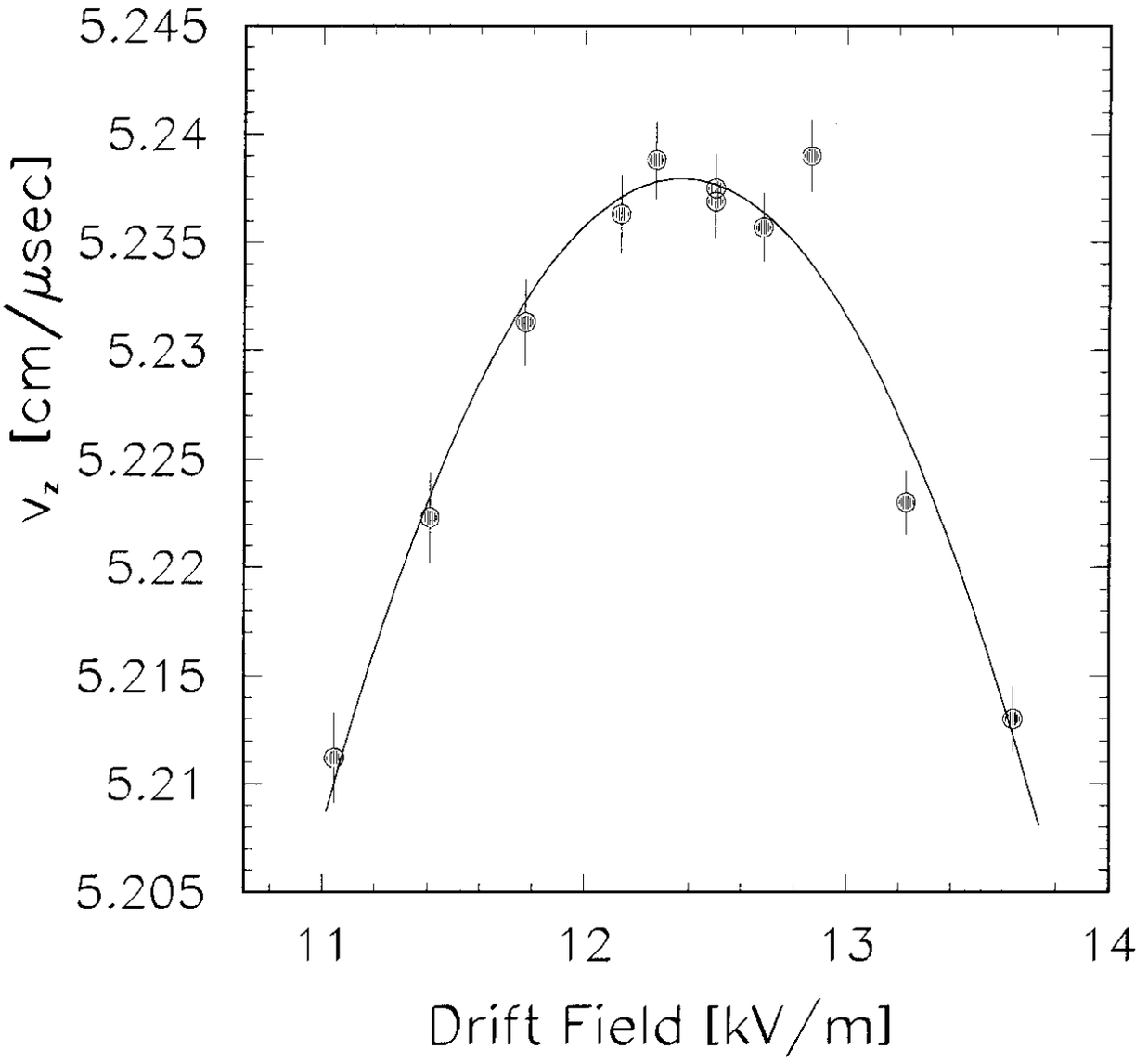

Figure 14: *Drift velocity as a function of the applied drift field.*

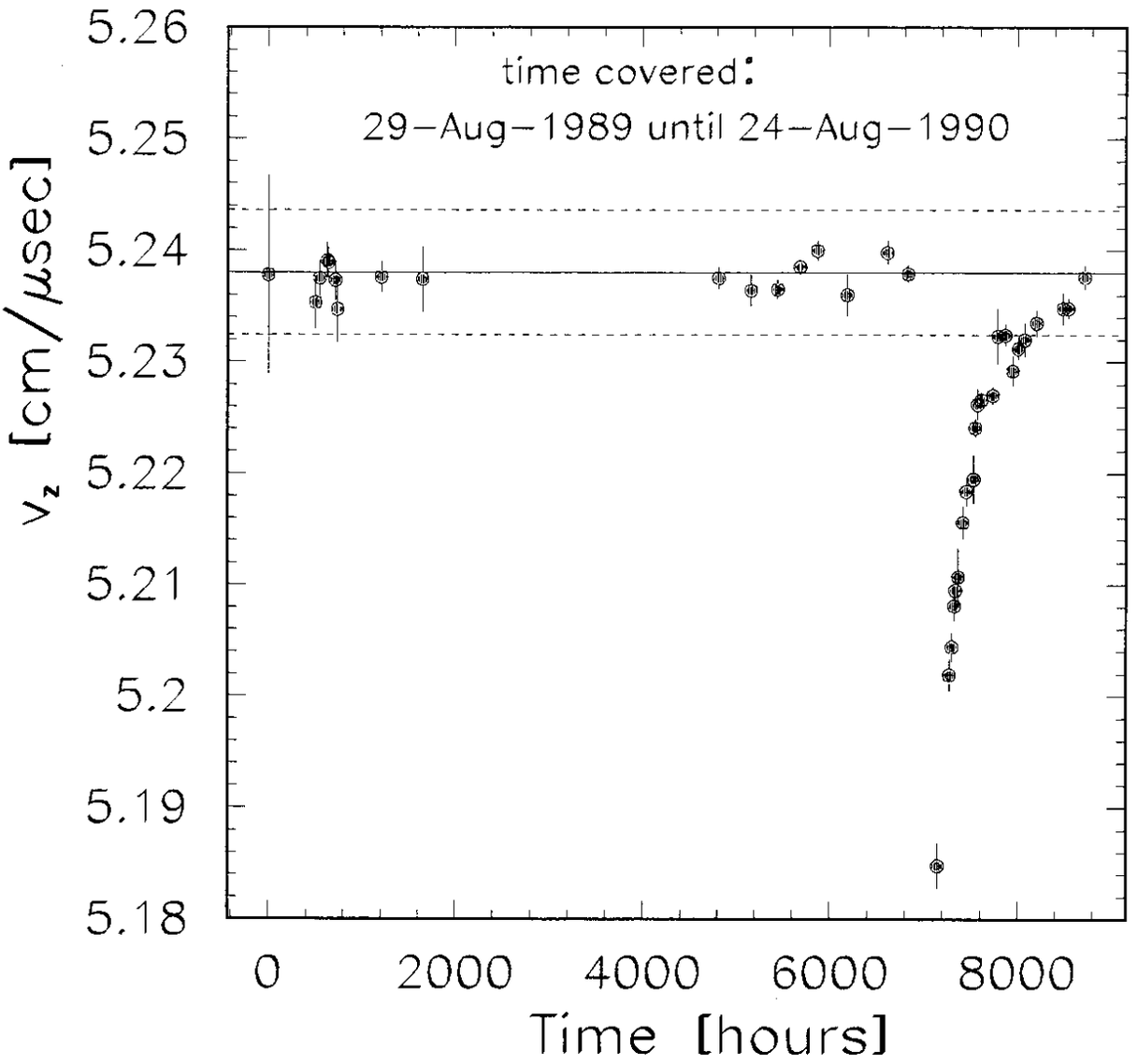

Figure 15: *Long-term monitoring of the drift velocity.*

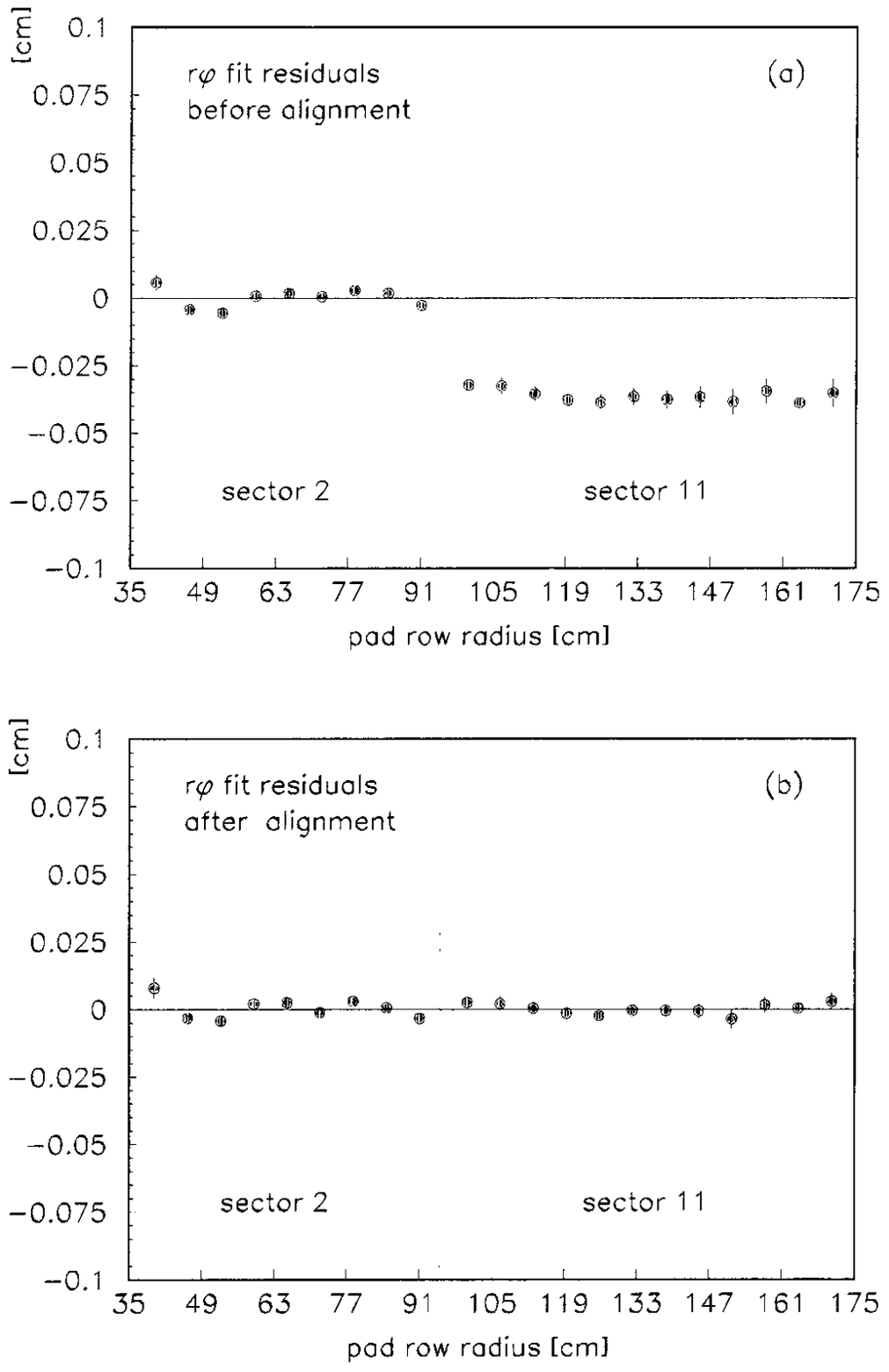

Figure 16: *Azimuthal fit residuals as a function of pad row radius for tracks fitted in an inner sector and extrapolated to an adjacent outer sector before and after alignment corrections. Here, the inner sector is labelled as sector 2 and the outer sector is labelled as sector 11.*

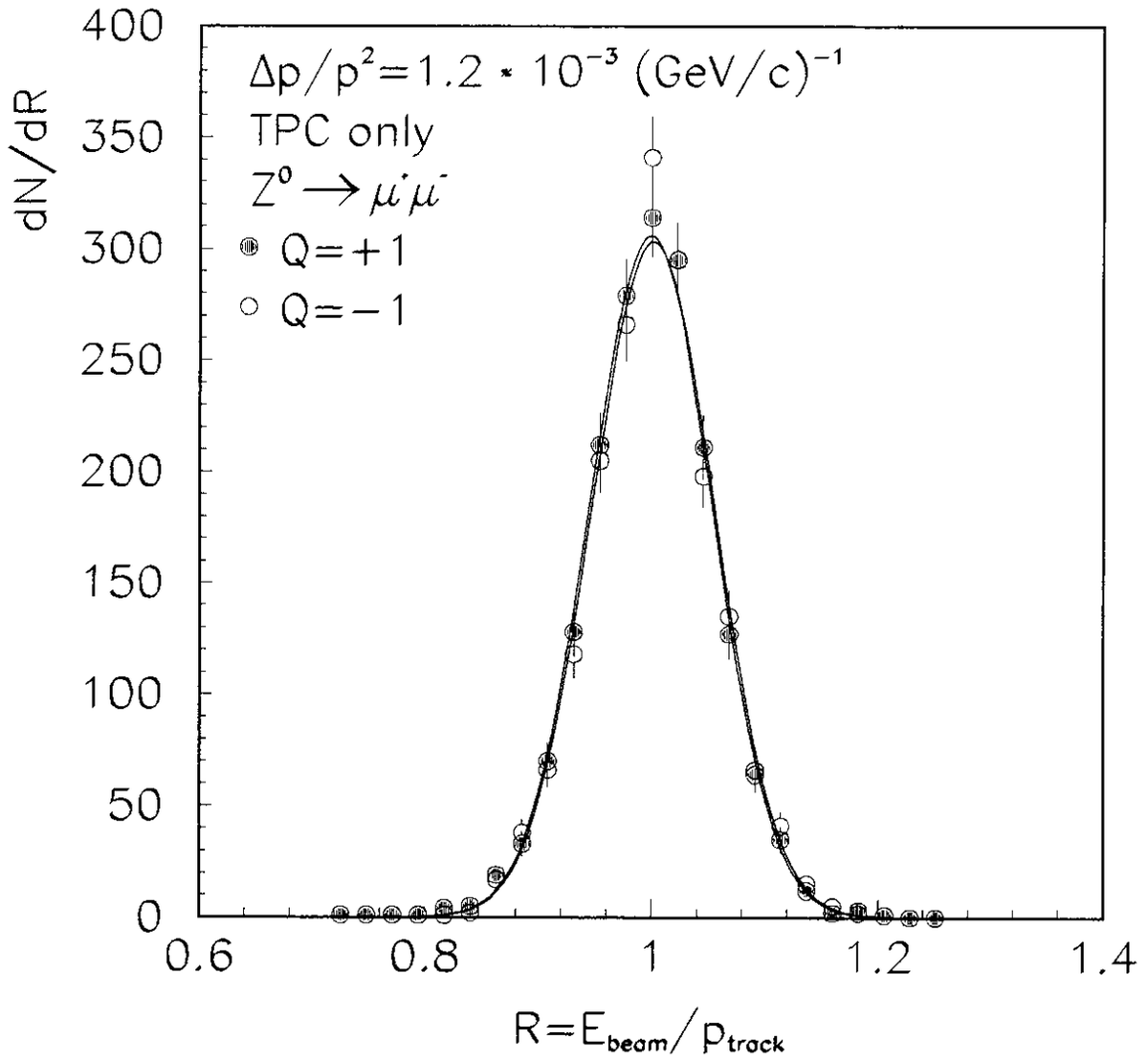

Figure 17: *The ratio beam energy over track momentum measured in the TPC for muons (charge Q) from* $Z^0 \rightarrow \mu^+\mu^-$ *decays.*

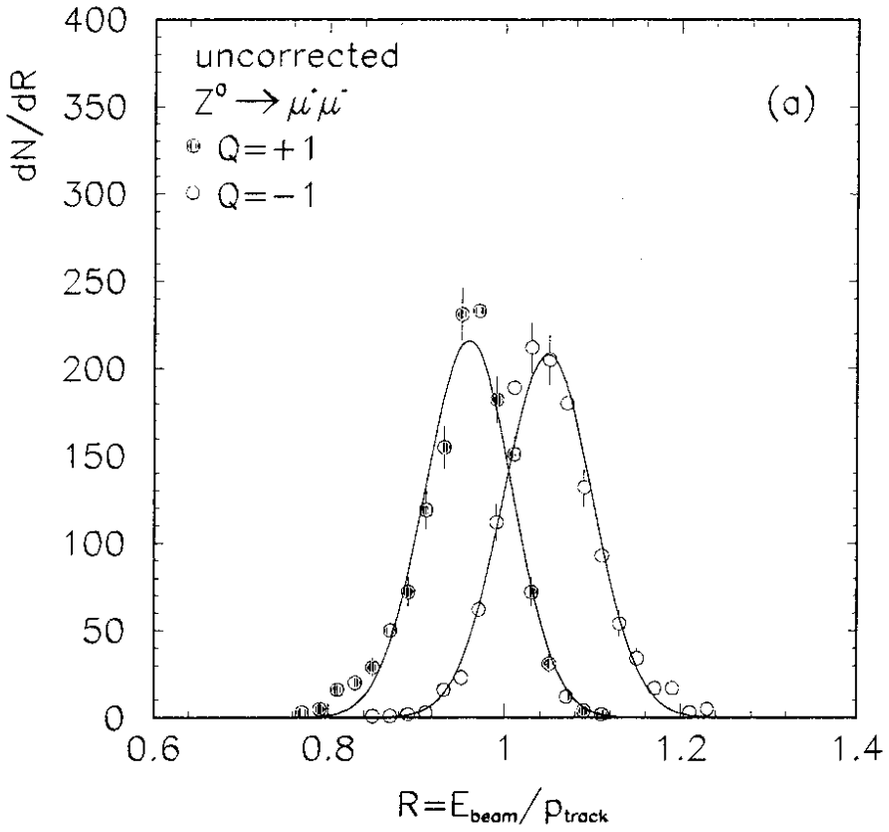

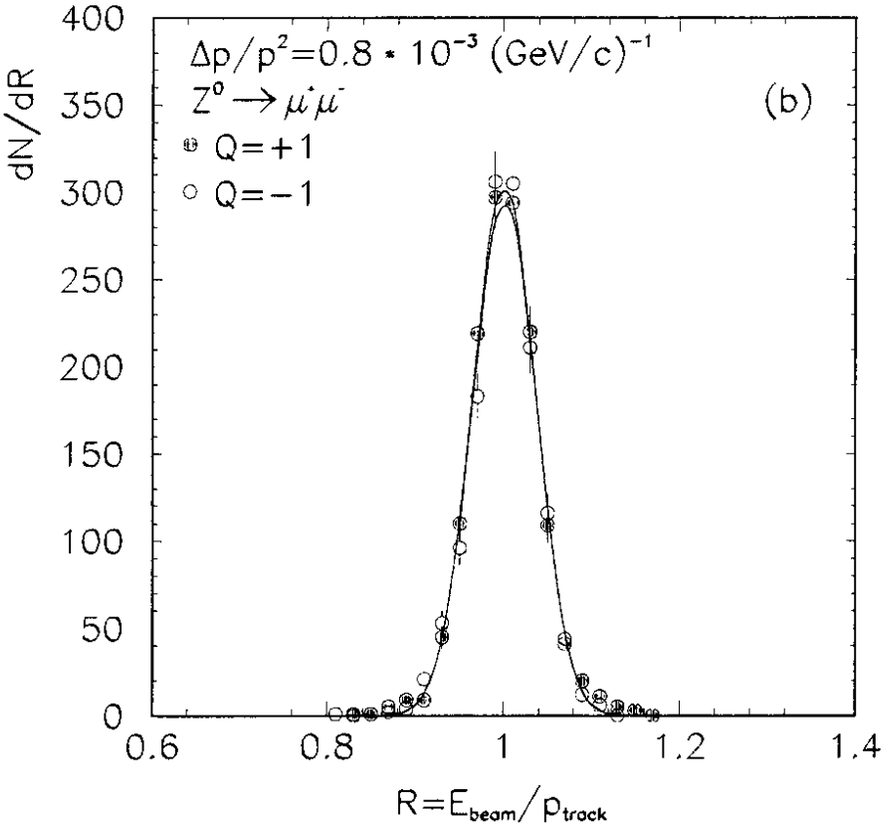

Figure 18: *The ratio beam energy over track momentum measured by ITC and TPC for muons (charge Q) from* $Z^0 \rightarrow \mu^+\mu^-$ *decays before and after correcting coordinates.*

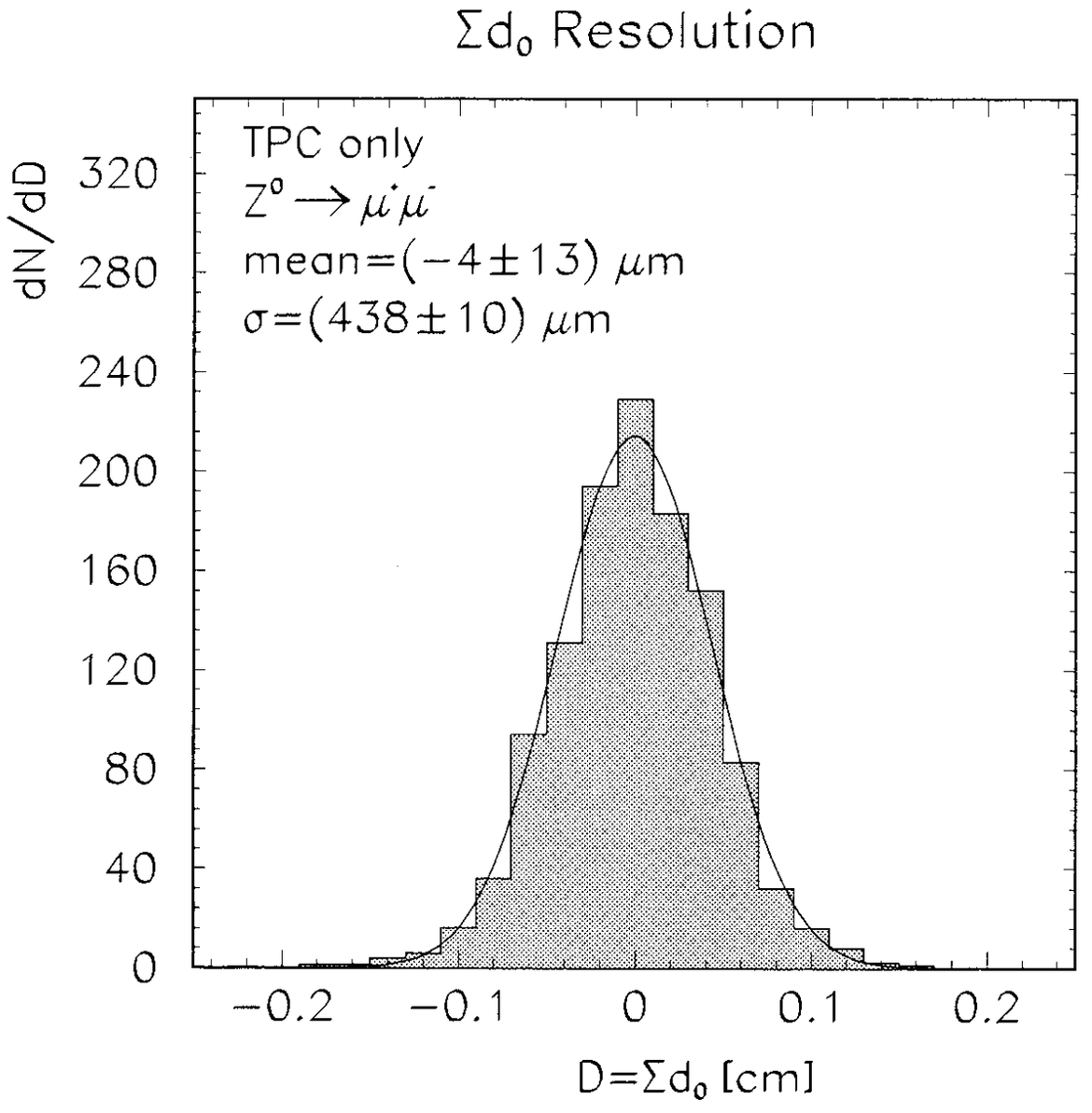

Figure 19: *Signed distance* Σd_0 *for* $Z^0 \rightarrow \mu^+\mu^-$ *decays.*

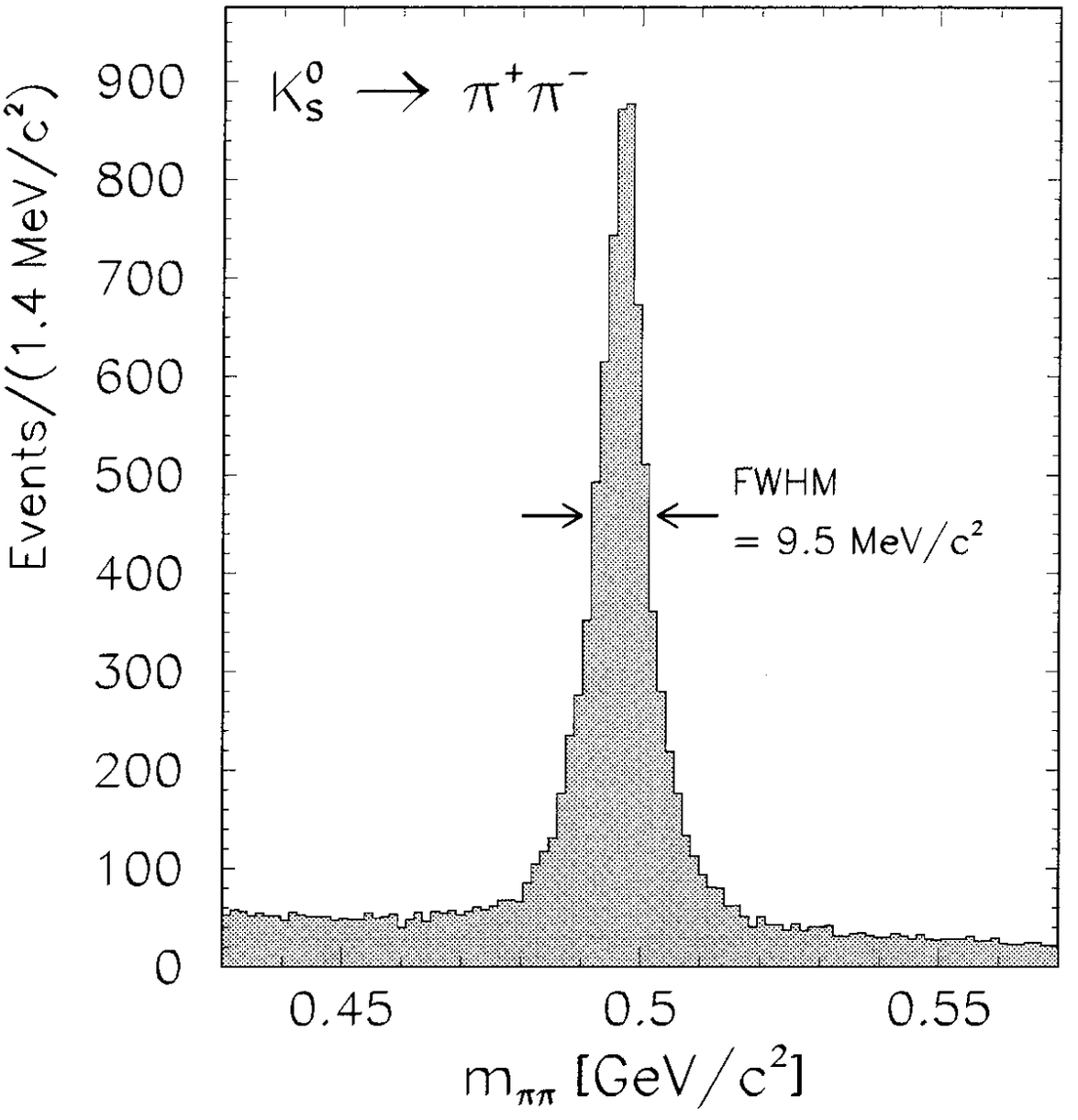

Figure 20: *Two-pion invariant mass distribution in hadronic Z^0 decays showing a peak at the K^0 mass.*

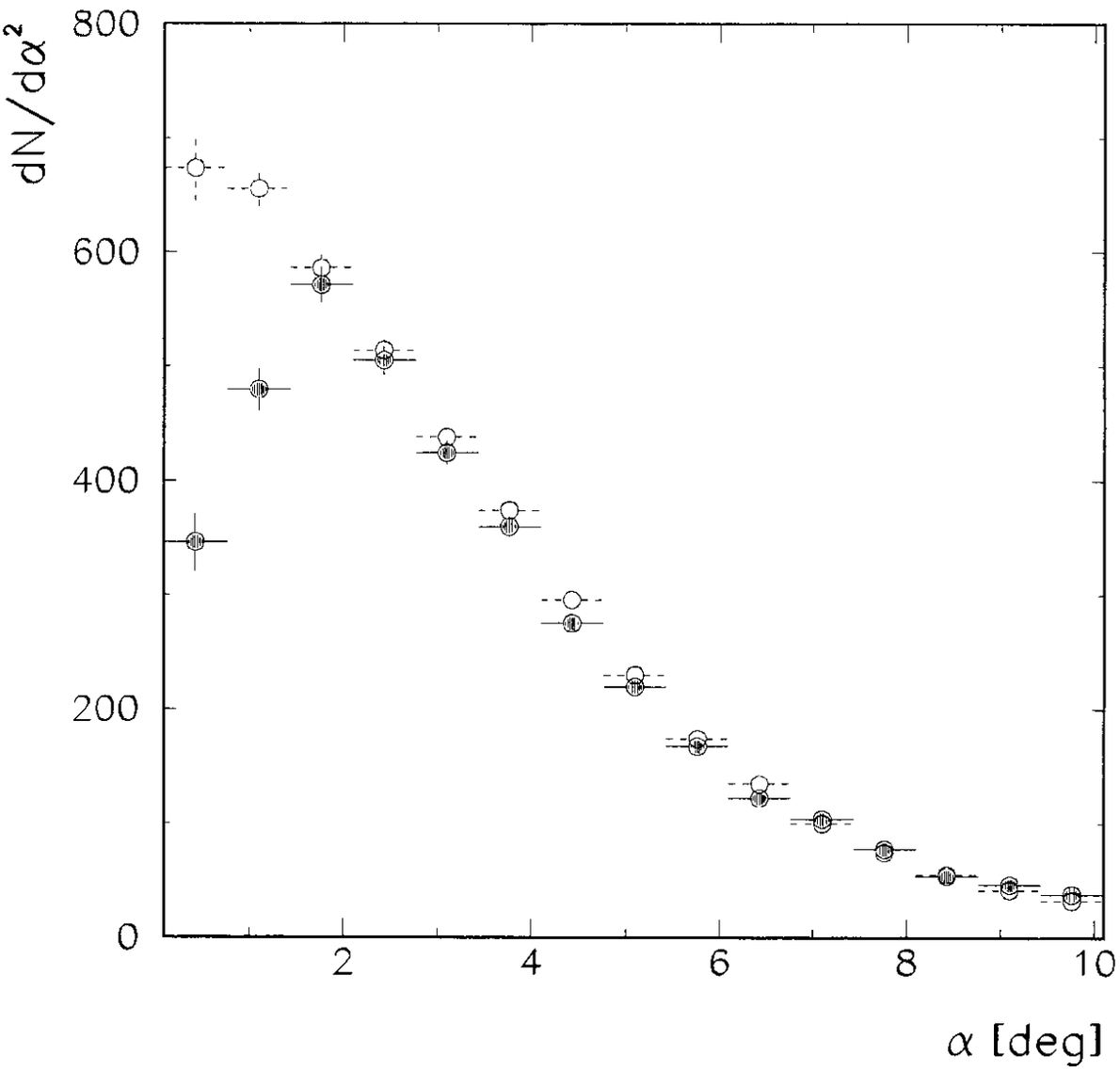

Figure 21: *$dN/d\alpha^2$ versus α for pairs of tracks of opposite sign charged particles (open circles) and same sign charged particles (full circles).*

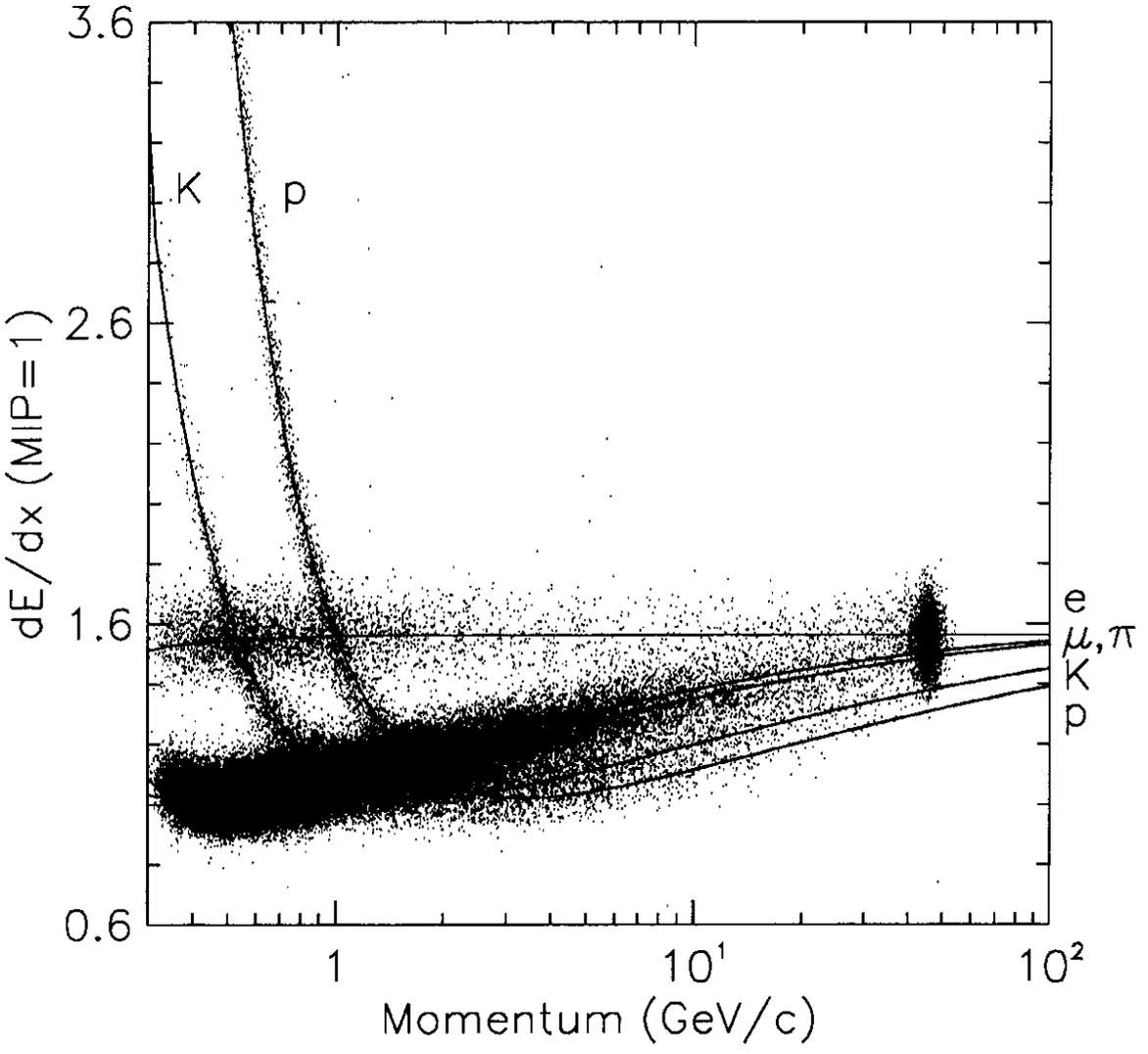

Figure 22: *A scatterplot of dE/dx versus momentum for all tracks with at least 150 dE/dx samples. The accumulation at high momentum is due to dilepton events, while the majority of the other tracks is from hadronic Z^0 decays. Overplotted is the fitted parameterisation of the most probable dE/dx as a function of momentum for each of five particle types. The dE/dx scale is arbitrarily normalised such that minimum-ionising particles have* $dE/dx \equiv 1$.